scientific reports

Check for updates

OPEN

A SWI/SNF complex-related genes signature predicts prognosis and immune infiltration in ccRCC with KCNK5 as a novel biomarker

Kai Xu[1,2,4], Zhiwei Yan[1,2,4], Yunxun Liu[1,2,4], Qiangmin Qiu[1,3], Xinmiao Ni[1,2], Hao Tang[1,2], Lei Wang[1,2]✉, Zhiyuan Chen[1,2]✉ & Xiuheng Liu[1,2]✉

Clear cell renal cell carcinoma (ccRCC) is the most common subtype of renal cell carcinoma (RCC). Although we have made many achievements in the therapy of RCC with the progress of medicine, the clinical management of metastatic RCC remains a daunting challenge. SWI/SNF chromatin remodeling complex-related genes (SCRGs) are significantly associated with tumor progression and cancer cell evolution in ccRCC. This study aimed to investigate the prognostic significance of SCRGs in ccRCC to elucidate its molecular subtype characteristics. Using 29 known SCRGs, 532 ccRCC patients from the TCGA-KIRC cohort were classified into two subtypes (SCRGcluster A and SCRGcluster B). Patients in SCRGcluster B exhibited a significantly poorer prognosis compared to those in SCRGcluster A. Functional enrichment and immune microenvironment profiles significantly differed between the subtypes, with SCRGcluster B showing higher levels of immune infiltration. Five core genes (*TMCC3*, *TOP2A*, *EPS8*, *PIK3R3*, *KCNK5*) were identified through the integration of multiple machine learning approaches and multivariate Cox regression analysis. A novel prognostic model based on these core genes was validated in an external cohort. Additionally, single-cell data analysis revealed the expression patterns of these core genes in ccRCC. In vitro experiments demonstrated that *KCNK5* is underexpressed in ccRCC cell lines and tissues, and that its overexpression suppresses malignant phenotypes. Specifically, *KCNK5* overexpression significantly inhibited the proliferation, migration, and invasion capabilities of ccRCC cell lines. Although the precise functional mechanisms of these core genes in ccRCC are not yet fully elucidated, this study provides new insights for the treatment of ccRCC.

Keywords CcRCC, SWI/SNF prognosis, Machine learning, Tumor microenvironment, Immunotherapy

Renal cell carcinoma (RCC) is the 14th most common cancer worldwide[1]. It is a malignant tumor that originates from renal epithelial cells, of which clear cell renal cell carcinoma (ccRCC) accounts for about 80%[2,3]. In recent years, due to the widespread use of abdominal imaging and the advancement of systemic therapy, the overall mortality rate has gradually decreased despite the increase in the incidence of RCC[4,5]. Currently, partial or radical nephrectomy is the preferred treatment for RCC limited to the kidney[6,7]. Although there have been advances in systemic therapy for metastatic RCC[8], because of the drug resistance of metastatic RCC and the high incidence of adverse reactions in combination therapies[9–12], nearly half of patients with metastatic RCC do not receive systemic treatment[13], which poses a huge challenge for the clinical management of RCC. Therefore, identifying new prognostic biomarkers for personalized risk assessment is crucial to advancing customized treatment methods for ccRCC.

SWI/SNF chromatin remodeling complexes (SCRCs) are large protein complexes encoded by 29 genes that can mobilize nucleosomes to regulate gene expression and participate in chromatin remodeling[14,15]. A growing number of studies have confirmed that SCRC-related genes (SCRGs) are associated with widespread genetic mutations in various cancers, indicating that SCRGs play a significant role in the development and metastasis of tumors. For example, a 1998 study observed that loss-of-function mutations of *SMARCB1* in Malignant

[1]Department of Urology, Renmin Hospital of Wuhan University, Wuhan 430060, Hubei, China. [2]Institute of Urologic Disease, Renmin Hospital of Wuhan University, Wuhan 430060, Hubei, China. [3]Department of Organ Transplantation, Renmin Hospital of Wuhan University, Wuhan 430060, Hubei, China. [4]Kai Xu Zhiwei Yan and Yunxun Liu are authors equally contributed. ✉email: drwanglei@whu.edu.cn; drchenzy@whu.edu.cn; drliuxh@whu.edu.cn

rhabdoid tumors can lead to tumourigenesis[16]. *ARID1A* mutations are frequently found in ovarian clear-cell and endometrioid carcinomas[17,18]. Researchers have identified truncating mutations of *PBRM1* in 41% of cases of ccRCC through high-throughput sequencing[19]. Deletion of *SMARCA4* can accelerate lung cancer progression and increase tumor invasiveness[20].

Meanwhile, researchers are also committed to finding targeted therapies against mutations of SCRGs to improve the clinical management of cancer. Targeted degradation of *SMARCA2/4* proteins mediated by proteolysis targeting chimeras (PROTACs) can induce rapid apoptosis of tumor cells, showing an anti-proliferative effect[21]. Given that SCRCs have an inverse genetic regulatory relationship with polycomb repressive complexes (PRCs)[14]. Several studies on *EZH2* inhibitors have shown that *EZH2* inhibitors suppress tumor progression by inhibiting *EZH2* activity and restoring the expression of tumor suppressor genes[22–25]. A recent pan-cancer study showed that SCRGs are differentially expressed in 13 tumor types and are closely related to prognosis. In addition, SCRGs are associated with regulating immune and tumor metastasis-related pathways and are particularly important for tumor progression and cancer cell differentiation in ccRCC[26]. In summary, numerous studies have demonstrated that SCRGs show great potential in cancer prognosis and treatment, providing new ideas for developing new prognostic biomarkers.

This study aims to identify the SCRG clusters and a prognostic signature in ccRCC through integrated bioinformatics analyses and machine learning algorithms, revealing their correlation with immune cell infiltration and immunotherapy. Bioinformatics plays a crucial role in cancer research and precision medicine, and is widely used to uncover potential molecular mechanisms and pathways involved in the initiation and progression of cancer[27]. However, no studies to date have utilized bioinformatics tools to investigate SCRG-related subtypes in ccRCC. Previous studies have demonstrated the significant influence of SCRGs on ccRCC prognosis and metastatic potential[28–32]. Moreover, most SCRGs exhibit distinct dysregulation patterns in ccRCC, and their expression levels are significantly associated with patient outcomes[26]. Based on these findings, we identified for the first time two SCRG clusters in ccRCC and developed a prognostic signature with strong predictive performance. Enrichment and immune infiltration analysis revealed potential associations among the SCRG prognostic signature, ccRCC prognosis assessment, immunotherapy, and the tumor microenvironment. This study fills a gap in SCRG-related subtyping among ccRCC patients and experimentally validates *KCNK5* as a potential novel prognostic biomarker for ccRCC. It provides preliminary evidence for further studies and lays a theoretical foundation for personalized treatment strategies.

Materials and methods

Data collection

Transcriptomic RNA sequencing data and corresponding clinical information were systematically retrieved from multiple public repositories. The TCGA-KIRC cohort we downloaded from The Cancer Genome Atlas (TCGA, https://portal.gdc.cancer.gov/) comprised 541 ccRCC and 72 normal tissue samples[33,34]. For external validation, we obtained the E-MTAB-1980 dataset (101 ccRCC samples) from ArrayExpress (https://www.ebi.ac.uk/arrayexpress) and transcriptomic profiles of 91 ccRCC patients from the International Cancer Genome Consortium (ICGC, https://dcc.icgc.org/)[35,36]. All datasets included expression data and survival information, with samples lacking survival data excluded from analysis. Clinical parameters from TCGA-KIRC encompassed age, gender, histological grade, pathological stage, and TNM classification (Table S1). The copy number variation and somatic mutation data for TCGA-KIRC were acquired through the UCSC Xena platform (https://xenabrowser.net). Four additional Gene Expression Omnibus (GEO, https://www.ncbi.nlm.nih.gov/geo/)[37] datasets were concurrently retrieved: GSE85258 (14 paired primary ccRCC/lung metastasis samples)[38], GSE40435 (101 tumor/normal paired samples)[39], GSE53757 (72 tumor/normal samples)[40], and GSE224630 (ScRNA-seq data from 7 specimens)[41].

It should be noted that owing to its large sample size and relatively comprehensive clinical data, the TCGA-KIRC dataset was selected to identify SCRG-based subtypes in ccRCC patients and to construct a prognostic model. The GSE85258 dataset, which includes paired primary and metastatic samples, was used to identify metastasis-associated differentially expressed genes. Additionally, GSE40435 and GSE53757, which consist of tumor and normal tissue pairs, provided further validation for differential expression analysis of the model genes. The GSE224630 single-cell RNA sequencing dataset was employed to explore tumor heterogeneity in ccRCC at the cellular level. Finally, E-MTAB-1980 (Table S2) and ICGC-KIRC (Table S3), both containing survival information (including survival time and status), were used to validate the generalizability of the prognostic model in external cohorts, ensuring that the results are not limited to a single dataset. All transcriptomic data underwent transcripts-per-million (TPM) normalization. The 29 SCRGs were obtained from previous studies[26], and the specific genes are shown in Table S4. Somatic mutation patterns were visualized through the 'maftools' R package[42], while chromosomal localization of SCRGs was mapped using the 'RCircos' R package. As all data were obtained from open-access databases in compliance with respective publication guidelines, no additional ethical approval was required for this study. The flow chart for this study is shown in Fig. S7.

Consensus clustering analysis based on SCRGs

Based on the expression analysis results of 29 SCRGs, we performed a consensus cluster analysis using the R package 'ConsensusClusterPlus' on 532 ccRCC patients from the TCGA-KIRC cohort and classified the patients into different clusters. The prognosis of different ccRCC clusters was demonstrated by survival analysis. We also used Gene Set Variation Analysis (GSVA) to explore the potential functions of SCRGs. To verify the differences among various ccRCC clusters through principal component analysis (PCA). In addition, we used the R pckage 'ESTIMATE' to calculate the ESTIMATE, immune, and stromal scores of different ccRCC clusters. Differences in the infiltration of 23 immune cells in ccRCC clusters were assessed by the CIBERSORT algorithm.

Development and validation of the SCRG prognostic signature

We screened for differentially expressed genes (DEGs) associated with prognosis by performing univariate regression analysis of DEGs between different ccRCC clusters in the TCGA-KIRC dataset. At the same time, we re-performed differential analysis of transcriptomic sequencing data from the GSE85258 dataset to identify genes associated with metastasis. To enhance predictive accuracy, we employed three advanced machine learning algorithms to construct prognostic models: LASSO regression[43], random forest (RF)[44], and extreme gradient boosting (XGBoost)[45]. We identified the intersection of the potential hub genes identified by the three algorithms, calculated the risk scores for each ccRCC patient in the training set, and divided the patients into high-risk and low-risk groups based on the median risk score. We evaluated the effectiveness and accuracy of the prognostic models using decision curve analysis (DCA)[46] and time-dependent receiver operating characteristic (ROC)[47] curves. To validate the risk assessment model, we also conducted studies on the test set and external datasets (E-MTAB-1980, ICGC-KIRC). Additionally, we developed a nomogram and plotted corresponding calibration curves to assess the predictive accuracy of the nomogram.

Clinical feature correlation analysis and functional enrichment analysis

We first investigated whether there were significant differences in risk scores among different SCRG clusters. Then we revealed the impact of risk scores on the prognosis of ccRCC patients through univariate and multivariate regression analysis. Based on the clinical feature data from the TCGA-KIRC cohort, we further investigated whether higher risk scores were associated with poorer prognosis. Additionally, we analyzed the expression patterns of immune checkpoint genes between high-risk and low-risk groups. We identified potential enriched pathways in the high-risk group using the gene set enrichment analysis (GSEA)[48]. We performed the Gene Ontology (GO) and Kyoto Encyclopedia of Genes and Genomes (KEGG)[49] enrichment analyses on the DEGs between the two groups to elucidate the biological processes (BP), molecular functions (MF), cellular components (CC), and potential signaling pathways associated with high-risk and low-risk groups in ccRCC.

Immune infiltration and tumor mutational burden analysis

We used multiple algorithms, including single-sample gene set enrichment analysis (ssGSEA), CIBERSORT[50], and ESTIMATE[51], to assess the distribution of immune cells in patients with ccRCC and to investigate the correlation between risk scores and tumor microenvironment (TME) immune infiltration. Based on previous studies[52], we explored the relationship between six pan-cancer immune subtypes (C1-C6) and risk scores. We studied the correlation between risk scores, immune-related functions, and TME scores. We also demonstrated the correlation between the expression levels of hub genes and immune cell infiltration. Additionally, we analyzed tumor mutational burden (TMB) in ccRCC patients, identifying the top 20 genes with the highest mutation frequencies across different risk groups. Patients were further divided into high-TMB (H-TMB) and low-TMB (L-TMB) groups to investigate the relationship between TMB grouping and patient prognosis. To provide new insights into ccRCC treatment, we scored patients in high-risk and low-risk groups using TIDE to predict the potential benefit of immunotherapy[53]. We also used the 'oncoPredict' package in R software to calculate the half-maximal inhibitory concentration (IC50) of commonly used drugs in patients with different risk scores, identifying potential drugs that could improve the prognosis of ccRCC patients[54].

Single-cell RNA sequencing data analysis

We analyzed the GSE224630 dataset using the Seurat package (v4.4.0) in R software[55]. Quality control was conducted on the single-cell RNA sequencing data by applying the following filtration criteria: (1) exclusion of cells containing fewer than 200 or more than 6,000 expressed genes; (2) removal of genes detected in fewer than 3 cells; and (3) elimination of cells with mitochondrial gene content exceeding 25%. The filtered dataset was normalized using the 'NormalizeData' function with a scale factor of 10,000, then identifying 3,000 highly variable genes through the 'FindVariableFeatures' function. Principal component analysis (PCA) was performed on these highly variable genes using the 'RunPCA' algorithm. To reduce batch effects between samples, we implemented data integration through the 'RunHarmony' function. Consistent with the original study methodology[41], we selected the top 30 principal components for subsequent analyses. Cellular clustering and dimensionality reduction were achieved using uniform manifold approximation and projection (UMAP) through the 'RunUMAP' function[56]. Finally, cell subpopulations within distinct clusters were annotated according to the original study's classification system.

Clinical sample collection and cell culture

We collected 5 pairs of tumor tissues and adjacent normal tissues from ccRCC patients who underwent radical or partial nephrectomy at the Renmin Hospital of Wuhan University between June 1, 2024, and November 30, 2024. This study was approved by the Renmin Hospital of Wuhan University Clinical Research Ethics Committee (approval number: WDRY2023-K176) and conducted in accordance with the Declaration of Helsinki. As the study was retrospective, it was exempt from informed consent requirements. The human renal proximal tubular epithelial cell line HK-2 and three ccRCC cell lines (786-O, 769-P, Caki-1) were acquired from the American Type Culture Collection (ATCC). HK-2 cells were cultured in Dulbecco's Modified Eagle Medium (DMEM; Procell Life Science & Technology, Wuhan, China) supplemented with 10% fetal bovine serum (FBS; Gibco, Grand Island, NY, USA) and 1% penicillin-streptomycin (Biosharp, Anhui, China). The ccRCC cell lines were propagated in RPMI-1640 medium (Procell Life Science & Technology) containing 10% FBS. All cell cultures were maintained under standard culture conditions at 37 °C in a humidified 5% CO_2 atmosphere.

Cell transfection

The recombinant plasmid expressing the human full-length *KCNK5* gene (pcDNA3.1-*KCNK5*) was custom-constructed by Sangon Biotech (Shanghai, China). An empty pcDNA3.1 vector was used as a negative control. Transfection was initiated when cells reached approximately 70% confluence using Lipofectamine 3000 transfection reagent (L300001, Thermo Fisher Scientific, USA) according to the manufacturer's protocol. Following a 48-hour incubation period post-transfection, successful overexpression of *KCNK5* was confirmed through Western blot analysis.

Western blot analysis

Protein extraction was performed using RIPA lysis buffer (Beyotime, P0013B, China) from cells and tissues. Protein concentrations were determined using a BCA protein assay kit (Beyotime, P0012S, China). Subsequently, protein samples were resolved by SDS-PAGE and electrophoretically transferred onto PVDF membranes (Millipore, USA). The membrane was then blocked with 5% non-fat milk for 1 hour, followed by overnight incubation with the primary antibody at 4 °C on a shaking incubator. Protein band visualization and quantification were performed using the ChemiDoc™ XRS+ imaging system coupled with ImageJ analysis software. The primary antibodies employed in this study included anti-*KCNK5* (Proteintech, 14136-1-AP, China) and anti-*GAPDH* (Proteintech, 10494-1-AP, China), the latter serving as a loading control.

Quantitative real-time reverse transcription polymerase chain reaction (qRT-PCR)

Total RNA was isolated from cell lines using TRIzol reagent (Invitrogen, USA) under RNase-free conditions. Following RNA extraction, cDNA synthesis was performed with the PrimeScript™ RT Kit (TaKaRa, Japan). Subsequently, qRT-PCR amplification was conducted using an A100 PCR system. The qRT-PCR was performed using TB Green PCT Master Mix (Akara, Japan) on a LightCycler 96 instrument. To ensure experimental reliability, both positive and negative controls were included in each run: no-template controls (NTCs) with nuclease-free water instead of cDNA template were used to detect potential contamination; no-reverse transcription controls (NRTs) were included to assess genomic DNA contamination. GAPDH served as the internal reference gene. Each sample was detected at least three times, and mRNA levels were quantified using the ΔΔCt method. Primer sequences utilized were as follows:

KCNK5: Forward 5′-CACTGGAAGGAGGCCAAGAA-3′, Reverse 5′-GACGGTCGCTGCAAAAATCA-3′

GAPDH: Forward 5′-GGAAGCTTGTCATCAATGGAAATC-3′, Reverse 5′-TGATGACCCTTTTGGCTC CC-3′.

Cell counting kit-8 (CCK-8) assay

We added approximately 5,000 cells to each well of 96-well plates and used the CCK-8 assay kit (Beyotime, Shanghai, China) to detect cell proliferation. After the cells were incubated for the specified time, CCK-8 solution was added, and the absorbance at a wavelength of 450 nm was measured according to the manufacturer's instructions.

5-ethynyl-2' -deoxyuridine (EdU) assay

Cell proliferation was further analyzed using the EdU assay kit (Beyotime, C0075S, China). Briefly, cells cultured in 12-well plates were sequentially stained with EdU reagent and Hoechst 33342 according to the manufacturer's protocol. Fluorescence imaging was performed using an inverted fluorescence microscope, and cell counting was performed using ImageJ software.

Wound healing assay

Cell migration was assessed using wound healing assays. Cells were seeded into a 6-well plate and cultured until they reached 100% confluence. A uniform wound was then created by scraping the cell layer along a straight line with a 200-μL pipette tip. After washing with PBS 2–3 times, microscopic images were captured at 0, 12, and 24 hours. The images were subsequently analyzed using ImageJ software.

Cell migration and invasion assay

The migration and invasion abilities of cells were further examined using a Transwell chamber (Beyotime, FTW061, China). In the migration assay, a cell suspension containing approximately 10,000 cells in serum-free medium was added to the upper chamber, while the lower chamber was filled with a medium containing high-concentration serum. After incubation for 24 hours in a cell culture incubator, the cells in the chambers were fixed with 4% paraformaldehyde and stained with 0.1% crystal violet solution. For the invasion assay, the upper chamber was pre-coated with a uniform layer of Matrigel™ matrix gel (Beyotime, C0372, China) at the bottom. The subsequent steps were identical to those in the migration experiment. Finally, images were captured using a microscope, and cell counting was performed with ImageJ software.

Statistical analysis

Statistical analyses were conducted using GraphPad Prism (v9.5.1) and R software (v4.3.1). Student's t-test was used to compare two groups, while one-way analysis of variance (ANOVA) was utilized for comparisons among three or more groups. A p-value < 0.05 was considered to indicate statistical significance, and * indicates p-value < 0.05, ** represents p-value < 0.01, and *** indicates p-value < 0.001. All experiments were repeated three times to ensure reliability.

Results

The genetic landscape of 29 SCRGs

Based on the transcriptome data from the TCGA database, the box plot (Fig. S1A) illustrated the expression levels of 29 SCRGs in normal and ccRCC samples, revealing significant differences in their expression between normal and tumor samples. The results of the waterfall plot (Fig. S1B) showed that 169 of the 357 ccRCC samples (47.34%) had mutations in the SCRGs, with *PBRM1* exhibiting the highest mutation frequency at 40%. The chromosomal locations of the 29 SCRGs appeared in Fig. S1C. In addition, as shown in Fig. S1D, *ACTL6A* had the highest amplification rate, while *PBRM1* and *SMARCC1* displayed the highest deletion rates. Correlation network plots (Fig. S1F, Fig. S1G) elucidated the interactions among the 29 SCRGs and highlight their prognostic significance in renal cancer patients. The results demonstrated that the majority of SCRGs were closely associated with the prognosis of renal cancer patients. The above results suggested that the 29 SCRGs may play a pivotal role in the development and prognosis of renal cancer.

Identification of two ccRCC clusters and analysis of potential functional pathways

Consensus clustering analysis (Fig. 1A, Fig. S2A–K) was applied to the 532 ccRCC samples from the TCGA database, resulting in the identification of two distinct clusters: Cluster A (n = 323) and Cluster B (n = 209). Principal component analysis (PCA) revealed significant differences between the clusters (Fig. S1E). Survival analysis demonstrated that patients in Cluster B exhibited a worse prognosis compared to those in Cluster A (Fig. 1B). The heatmap in Fig. 1C illustrated the correlation between the expression levels of 29 SCRGs and the clinicopathological characteristics of ccRCC samples. The ssGSEA was employed to investigate the differences in the infiltration of 22 immune cell types between the two ccRCC clusters. The results indicated that nearly all immune cell infiltrations were significantly higher in Cluster B (Fig. 1D), suggesting that immune pathways may play a crucial role in the pathogenesis of ccRCC. Furthermore, the ESTIMATE algorithm analysis revealed that the ESTIMATE score (Fig. 1E), immune score (Fig. 1F), and stromal score (Fig. 1G) were all higher in Cluster B compared to Cluster A, further highlighting the unique immune and stromal features of Cluster B.

Following consensus clustering analysis, we conducted gene set variation analysis (GSVA) on TCGA cohort samples to elucidate pathway enrichment patterns between molecular subtypes. The GSVA revealed distinct pathway activation profiles: Cluster B demonstrated significant enrichment in allograft rejection, epithelial-mesenchymal transition (EMT), and *IL-6/JAK/STAT3* signaling pathways. Conversely, Cluster A exhibited predominant activation of bile acid metabolic, UV response DN, and protein secretion processes (Figure 2A). Through difference analysis (adjusted $p < 0.05$, $|\log FC| > 2$), we identified 2579 DEGs between the two clusters (Figure S2L). Subsequent stringent filtering ($p < 0.001$) followed by univariate Cox regression analysis revealed 1157 survival-associated DEGs with significant prognostic value (Table S5). The top 50 most significant survival-related genes were visualized using a forest plot to illustrate their hazard ratios and confidence intervals (Figure 2B).

To elucidate the potential functional pathways associated with these DEGs, we conducted the GO and KEGG analysis comprehensively. The GO analysis revealed that these DEGs were primarily enriched in proteasome-mediated ubiquitin-dependent protein catabolic process, cellular component disassembly, ras protein signal transduction, regulation of cell-matrix adhesion, focal adhesion, cell-substrate junction, cell leading edge, lamellipodium, cadherin binding, growth factor binding, actin binding, vitamin binding and other functions (Fig. 2C). The KEGG analysis further illuminated the involvement of these DEGs in various metabolic and signaling pathways. The results indicated that these DEGs were mainly involved in valine, leucine and isoleucine degradation, salmonella infection, fatty acid degradation, carbon metabolism, adherens junction, proteoglycans in cancer, tryptophan metabolism, focal adhesion, FoxO signaling pathway, EGFR tyrosine kinase inhibitor resistance, fatty acid metabolism, yersinia infection, shigellosis, protein processing in endoplasmic reticulum, regulation of actin cytoskeleton, etc (Fig. 2D).

To further investigate the molecular mechanisms underlying ccRCC metastasis, we conducted a differential expression analysis using transcriptome sequencing data from 14 pairs of primary ccRCC tumors and patient-matched lung metastasis samples obtained from the GSE85258 dataset. The volcano plot (Fig. 2E) illustrated that 451 genes exhibited significant differences in expression levels between the primary tumors and metastatic samples ($p < 0.05$, $|\log FC| > 0.585$). These genes were named metastasis-related genes. Subsequently, we intersected these 451 metastasis-related genes with the previously identified 1157 DEGs associated with ccRCC survival. This analysis revealed 78 overlapping genes (Fig. 2F), which may represent key molecular players involved in both ccRCC progression and metastasis.

Development and validation of the SCRG prognostic signature based on multiple machine learning algorithms

To mitigate the risk of overfitting and minimize the impact of noise in the data, we partitioned the 532 ccRCC patients from the TCGA cohort into a training set (n = 268) and a test set (n = 264) at an approximate 1:1 ratio. Utilizing the training set data, we employed three machine learning algorithms—LASSO, XGBoost, and Random Forest (RF)—to screen for 10, 15, and 30 genes, respectively, from the 78 overlapping genes (Fig. 3A–F). By intersecting the results obtained from these three algorithms, we ultimately identified five hub genes to construct the SCRG prognostic signature (Fig. 3G):

SCRG risk score=(−0.05951×*TMCC3* expression)+(0.040301×*TOP2A* expression)+(−0.03749×*EPS8* expression)+(−0.03833×*PIK3R3* expression)+(−0.0393×*KCNK5* expression)

We calculated the risk scores for all ccRCC patients in the training and validation sets and categorized the patients in each cohort into high-risk and low-risk groups based on the median score. In the training set, survival analysis and survival status plots revealed that patients in the high-risk group had a worse prognosis and higher mortality (Fig. 3H–J). A heatmap depicting the differential expression of the five signature genes

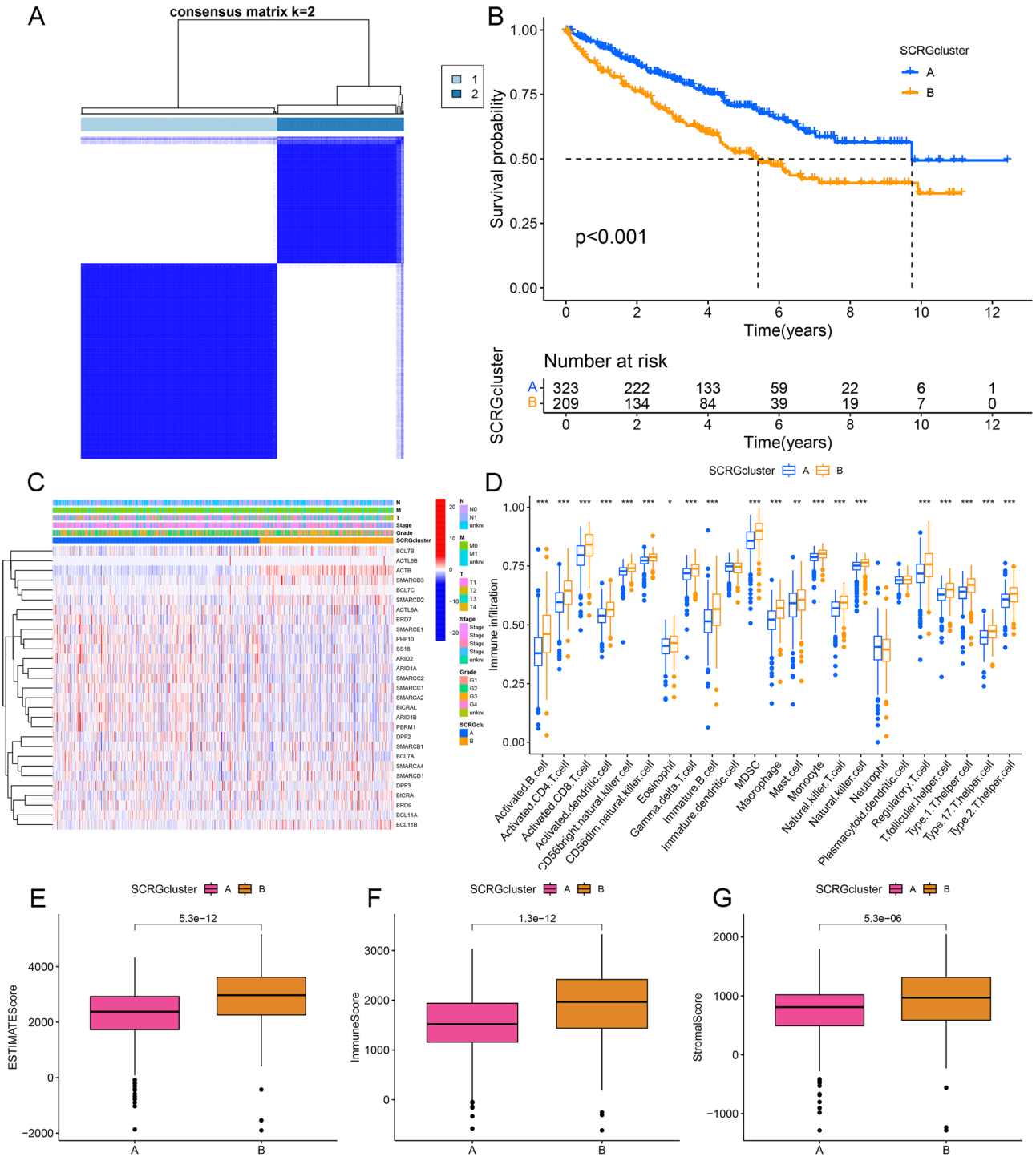

Figure. 1. Identification of two SCRG clusters. (**A**) Optimized κ ensures consistent clustering effects among samples. (**B**) Survival analysis comparing the two SCRG clusters. (**C**) Heat map of gene expression profiles, annotated with histological grade, pathological stage, TNM stage, and SCRG cluster. (**D**) Immune cell infiltration patterns linked to SCRG clusters. (**E–G**) Differences in ESTIMATE score (**E**), immune score (**F**), and stromal score (**G**) between the two SCRG clusters.

showed that, except for *TOP2A*, which was highly expressed in the high-risk group, the remaining four genes were expressed at lower levels in the high-risk group (Fig. 3K). The receiver operating characteristic (ROC) curve analysis demonstrated that the area under the curve (AUC) values for the training set at 1, 3, and 5 years were 0.780, 0.764, and 0.726, respectively, indicating that our SCRG prognostic signature has reliable accuracy in predicting the survival time of patients with ccRCC (Fig. 3L). These conclusions were further validated in the

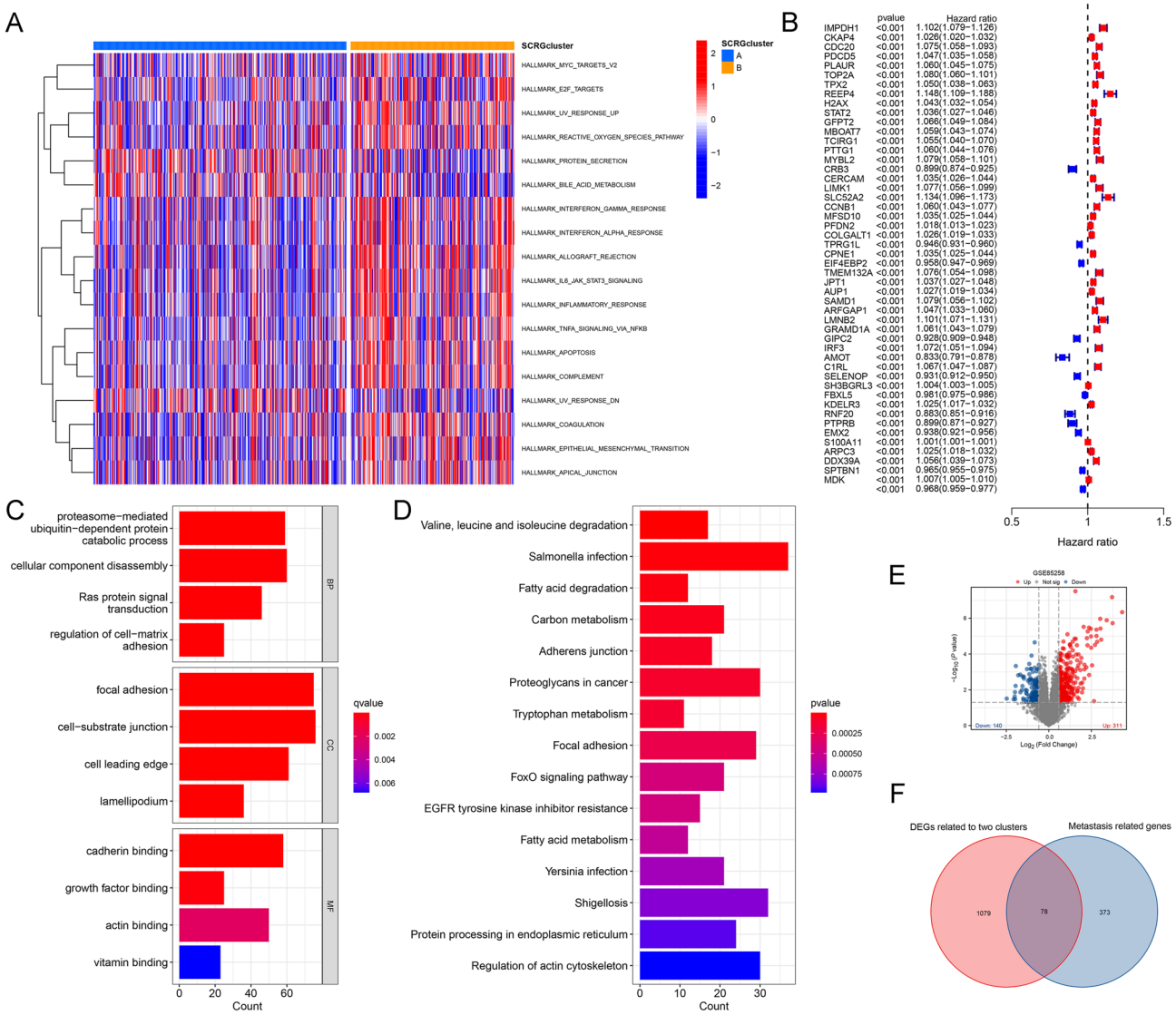

Figure. 2. Analysis of potential pathways and DEGs linked to SCRG clusters. (**A**) GSVA evaluation of hallmark gene set activity across distinct SCRG clusters. (**B**) Forest plot of the top 50 DEGs most associated with ccRCC patient survival. (**C–D**) GO (**C**) and KEGG (**D**) functional enrichment analyses of DEGs. We obtained permission from the Kanehisa laboratory to use KEGG images[84–86]. (**E**) Volcano plot of DEGs between primary ccRCC and matched lung metastasis samples. (F) Venn diagram of co-expressed genes between SCRG cluster-associated DEGs and metastasis-associated DEGs.

test set and external validation datasets (E-MTAB-1980, ICGC-KIRC), and the results were consistent with those observed in the training set (Fig. S3A–C).

Additionally, we developed a nomogram (Fig. 3N) incorporating gender, risk score, age, and pathological stage to facilitate clinicians' prediction of ccRCC patient survival. The accuracy of this nomogram was confirmed through ROC curve analysis (Fig. 3M) and decision curve analysis (DCA) (Fig. 3O), with an AUC value of 0.864. This conclusion was also corroborated by the calibration curve (Fig. 3P).

The biological status and tumor immune microenvironment landscape of different SCRG risk scores

The Sankey diagram depicted the differences in risk stratification and survival status among patients from the two SCRG clusters (Fig. 4A). The visualization demonstrated that cluster A predominantly comprised low-risk patients, while cluster B had a higher proportion of high-risk patients (Fig. 4B). This finding was further corroborated by the box plot, which revealed that the risk scores of patients in cluster B were significantly higher than those in cluster A (Fig. 4C).To establish the risk score as an independent prognostic factor, we conducted univariate and multivariate regression analyses. These analyses confirmed that the risk score, pathological stage, and histological grade are significant independent prognostic factors for patients with ccRCC (Fig. 4D–E). Moreover, the heat map and box plot results indicated a close association between the risk score and the advanced

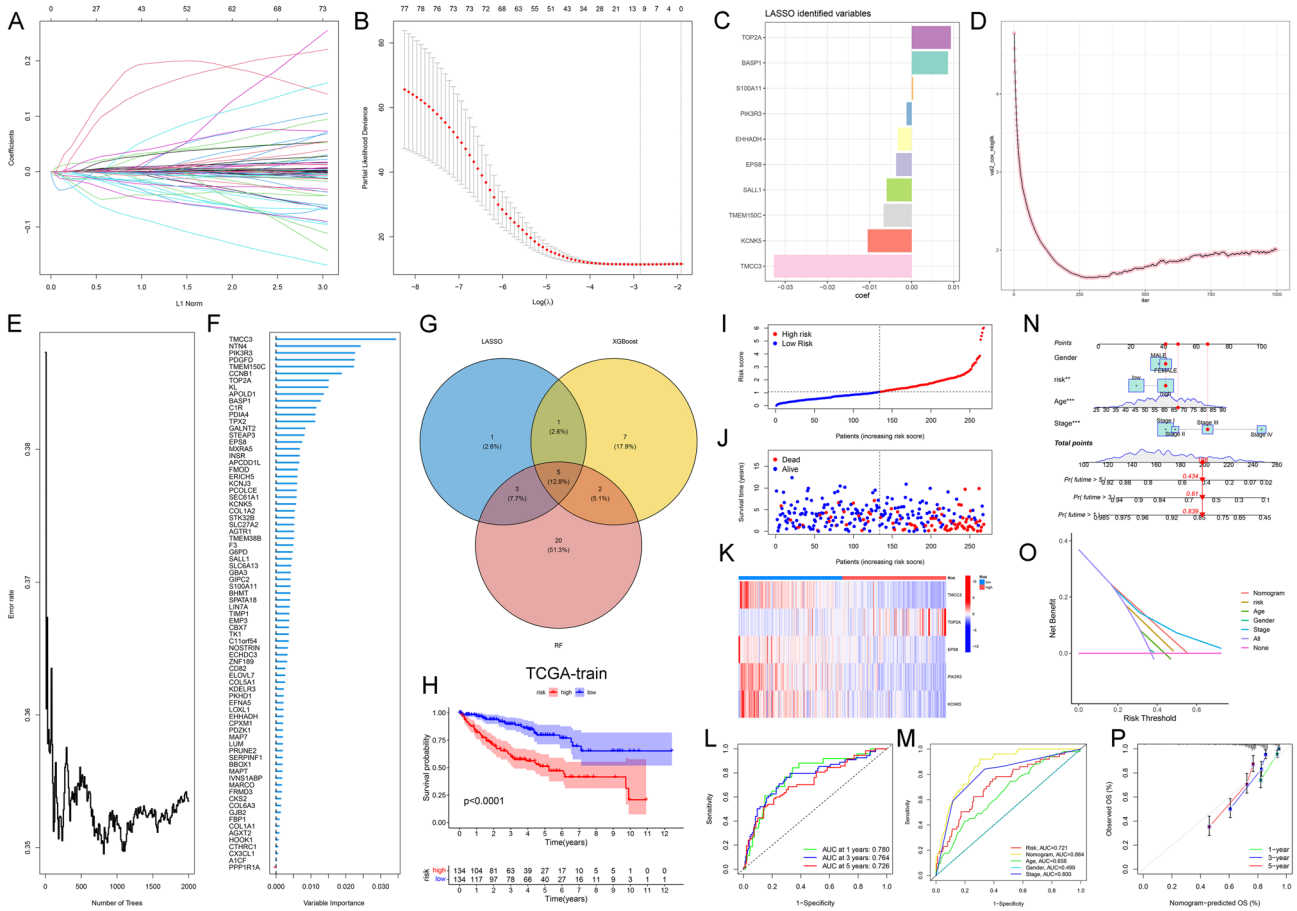

Figure. 3. Identification of key genes and construction of a prognostic model using machine learning algorithms. (**A–C**) Identification of key genes via LASSO regression analysis. (**D**) Identification of key genes using the XGBoost algorithm. (**E–F**) Identification of key genes via the RF algorithm. (**G**) Venn diagram of the intersection of key genes identified by three machine learning algorithms. (H) Survival analysis of high-risk and low-risk groups in the TCGA-train cohort based on the median risk score. (**I**) Distribution of risk scores in high-risk and low-risk groups in the TCGA-train cohort. (**J**) Distribution of survival status in high-risk and low-risk groups in the TCGA-train cohort. (**K**) Heatmap of expression levels of the five model genes in high-risk and low-risk groups in the TCGA-train cohort. (**L**) ROC curves of the prognostic model for predicting 1-, 3-, and 5-year overall survival rates of ccRCC patients in the TCGA-train cohort. (**M**) AUC values of risk scores, nomogram, and other clinical features. (**N**) Nomogram predicting 1-, 3-, and 5-year overall survival rates of ccRCC patients based on risk scores and clinical features. (**O**) DCA curves of the nomogram, risk scores, and other clinical features. (**P**) Calibration curves of the nomogram at 1, 3, and 5 years.

clinical stage. Patients with higher pathological stages and histological grades have higher scores, while there is no significant difference in age (Fig. 4F–H).Differential analysis of the 47 immune checkpoint-related genes revealed that the expression of immune checkpoints was significantly upregulated in the high-risk group. This suggests the potential presence of immune escape in these patients (Fig. 4I). Additionally, the tumor immune dysfunction and exclusion (TIDE) analysis results showed that the TIDE score was higher in the high-risk group, further indicating a higher likelihood of immune escape in this group (Fig. S4F).

To elucidate the molecular mechanism by which the SCRG risk score affects patient prognosis, we found that the SCRG risk score is mainly associated with functions and pathways such as immune response, inflammation, coagulation, extracellular matrix regulation, and molecular metabolism. Specifically, the GSEA revealed that the SCRG score was positively correlated with the activation of pathways associated with malignant tumors (such as coagulation, EMT, E2F targets, and G2M checkpoint) and immune pathways (Fig. 4J).Based on the DEGs identified in different risk groups, the GO analysis showed that these genes were mainly enriched in processes such as immunoglobulin production, production of molecular mediators of immune response, acute inflammatory response, acute-phase response, regulation of hemostasis, fibrinolysis, humoral immune response, regulation of blood coagulation, antimicrobial humoral response, negative regulation of hemostasis, and various cellular components and molecular functions (Fig. 4K).The KEGG analysis further revealed that these DEGs were primarily enriched in pathways such as complement and coagulation cascades, viral protein interaction with cytokine and cytokine receptor, mineral absorption, cytokine-cytokine receptor interaction, cholesterol metabolism, fat digestion and absorption, PPAR signaling pathway, rheumatoid arthritis, NF-kappa B signaling

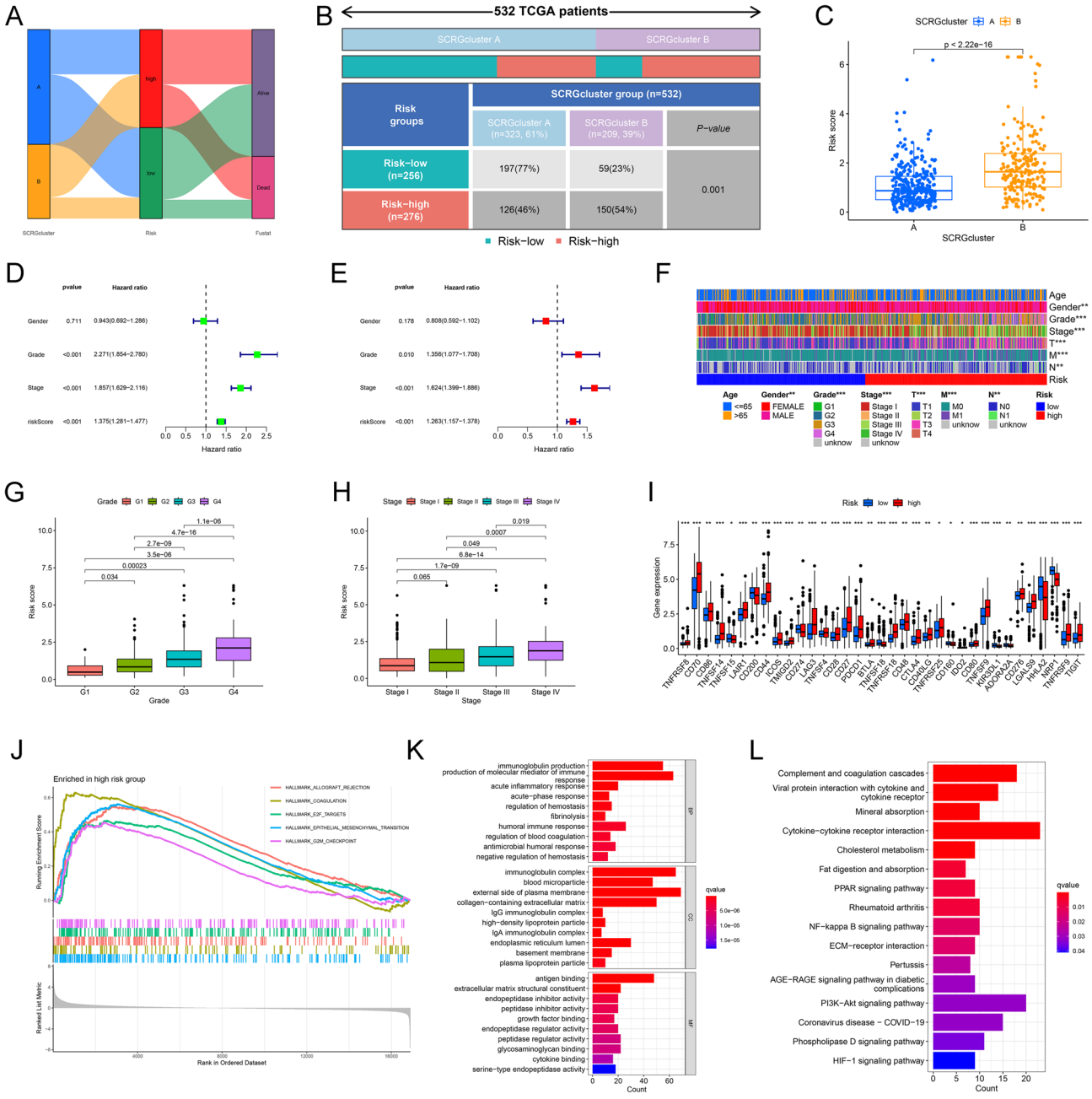

Figure. 4. Prognostic and functional enrichment analysis of the SCRG risk assessment model. (**A**) The Sankey diagram illustrates differences in risk stratification and survival status between the two SCRG clusters. (**B**) Cluster A is mainly low-risk, whereas cluster B has a higher proportion of high-risk patients. (**C**) Box plots confirm the differences in risk scores between the two clusters. Univariate (**D**) and multivariate (**E**) regression analyses indicate that risk scores, pathological stage, and histological grade are independent prognostic factors. (**F**) Heatmaps show differences in age, gender, histological grade, and pathological stage between high-risk and low-risk groups. Patients with higher histological grade (**G**) and pathological stage (**H**) tend to have higher risk scores. (**I**) The expression of immune checkpoint genes was significantly upregulated in the high-risk group. (**J**) GSEA enrichment analysis in the high-risk group. GO (**K**) and KEGG (**L**) enrichment analyses of DEGs between high-risk and low-risk groups (We obtained permission from the Kanehisa laboratory to use KEGG images[84–86].

pathway, ECM-receptor interaction, pertussis, AGE-RAGE signaling pathway in diabetic complications, PI3K-Akt signaling pathway, coronavirus disease-COVID-19, phospholipase D signaling pathway, and HIF-1 signaling pathway (Fig. 4L).

A comprehensive analysis of the association between risk scores and TME immune infiltration in ccRCC revealed significant immunological patterns. Through multi-algorithm integration (CIBERSORT, XCELL,

TIMER, QUANTISEQ, MCPCOUNTER, EPIC, and CIBERSORT-ABS), we identified distinct immune cell correlations: risk scores demonstrated positive associations with T cells CD8, T cells follicular helper, T cells regulatory(Tregs) while showing inverse relationships with T cells CD4 memory resting, monocytes, macrophages M1, mast cells resting (Figure 5A, C, G-I). ESTIMATE algorithm decomposition further revealed that high-risk patients exhibited significantly elevated immune and ESTIMATE scores compared to low-risk counterparts, though stromal scores showed no intergroup difference (Figure 5B). Immune function enrichment analysis delineated distinct activation patterns between risk groups. The high-risk group was enriched in APC-co-inhibition, APC-co-stimulation, CCR, checkpoint, cytolytic activity, HLA, inflammation-promoting, parainflammation, T cell-co-inhibition, and T cell-co-stimulation. Conversely, low-risk patients showed predominant activation of Type-II-IFN response (Figure 5D). Immune subtype stratification analysis revealed the inflammatory C3 subtype harbored the lowest risk scores, while the tissue-reparative C1 subtype showed maximal risk scores (Figure 5E). Notably, the five hub genes were also significantly associated with immune cell infiltration (Figure 5F). These multimodal findings suggest that while an elevated SCRG risk score correlates with increased immune infiltration density, this infiltrate appears functionally compromised—characterized by coexisting effector cell populations and suppressive regulatory elements. This paradoxical immune signature may underlie the clinical aggressiveness associated with high-risk ccRCC phenotypes.

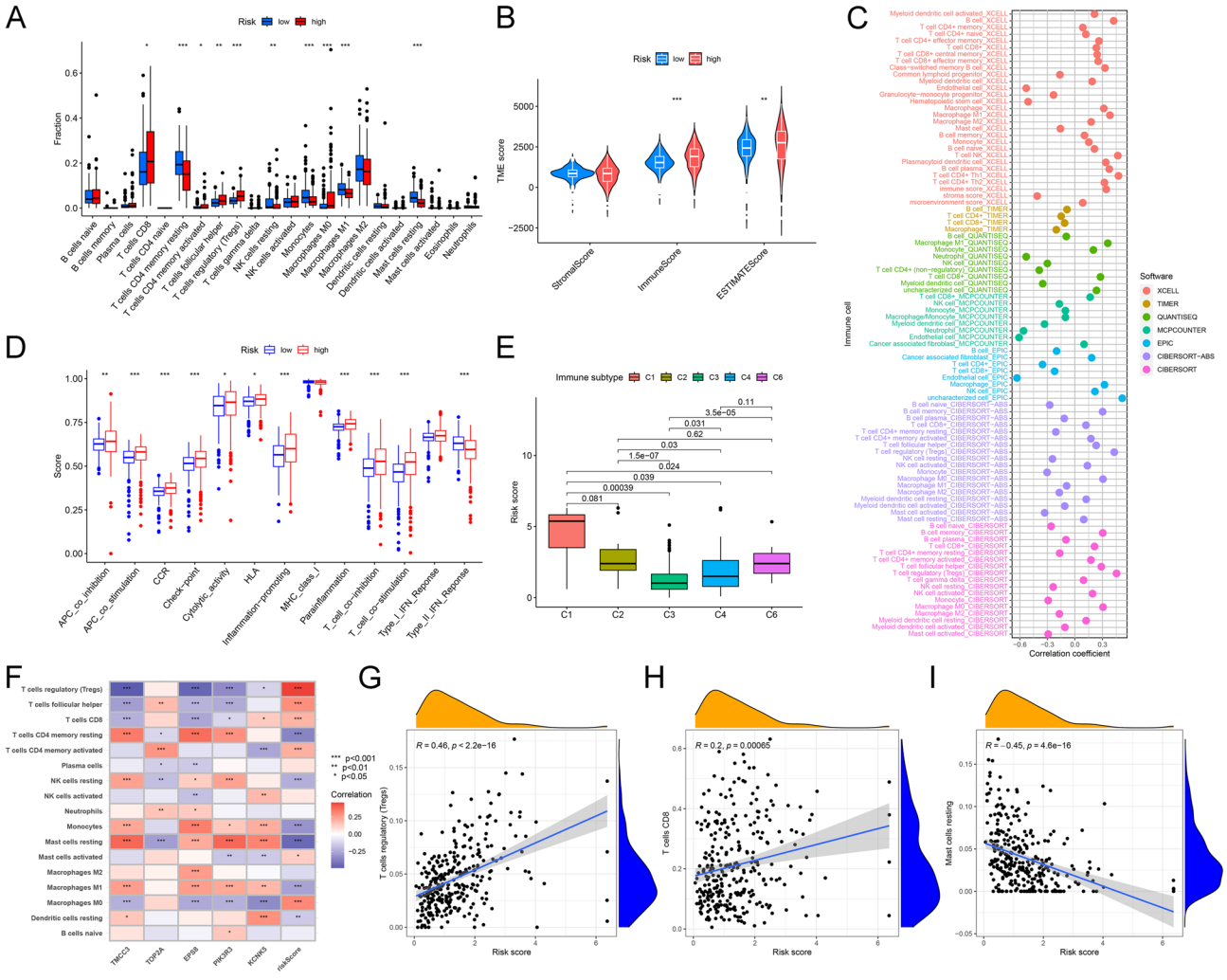

Figure. 5. Correlation analysis of risk scores with tumor microenvironment immune features in ccRCC. (**A**) Box plots display differences in tumor microenvironment cell type proportions between high-risk and low-risk groups. (**B**) The ESTIMATE algorithm shows that the immune and ESTIMATE scores are significantly higher in the high-risk group, while the stromal score exhibits no statistical difference. (**C**) Multi-algorithm integration analysis indicates the correlation between risk scores and immune cell infiltration. (**D**) Differences in immune-related functions between high-risk and low-risk groups. (**E**) Distribution of immune subtypes in high-risk and low-risk groups. (**F**) Correlation analysis of model genes with immune cells. Scatter plots illustrate correlations between risk scores and Tregs (**G**), CD8 T cells (**H**), and resting mast cells (**I**).

Tumor mutation burden and drug sensitivity with different SCRG risk scores

Tumor mutation burden (TMB) serves as an indirect indicator of the capacity and extent to which tumors generate neoantigens, and it has been demonstrated to predict the efficacy of immunotherapy across various tumor types. The results of somatic mutation analysis (Fig. S4A-B) revealed that the genes with the highest mutation frequencies in the high-risk group were *VHL* (41%), *PBRM1* (36%), *TTN* (19%), *SETD2* (14%), and *BAP1* (14%). In the low-risk group, the most frequently mutated genes were *VHL* (42%), *PBRM1* (38%), *TTN* (12%), *SETD2* (8%), and *DNAH9* (7%). The RNA-based stemness score (RNAss) analysis showed a positive correlation between the risk score and RNAss (Fig. S4C), suggesting that higher risk scores are associated with lower cellular differentiation and higher tumor malignancy. Additionally, we found that patients in the H-TMB group had worse prognoses compared to those in the L-TMB group (Fig. S4D). As anticipated, the subgroup with high TMB and high risk (H-TMB+high risk) exhibited the worst prognosis among all subgroups (Fig. S4E).

To identify potential therapeutic drugs for ccRCC patients, we evaluated commonly used drugs in clinical practice. Drug sensitivity analysis, based on the half-maximal inhibitory concentration (IC50), was employed to assess drug sensitivity, and over 100 drugs with varying sensitivities were screened. For simplicity, we selected only eight drugs for presentation. In the low-risk group, the IC50 values of erlotinib, gefitinib, ibrutinib, osimertinib, ruxolitinib, and ulixertinib were significantly lower than those in the high-risk group, indicating that these drugs may be more effective in the low-risk group. Conversely, dasatinib and lapatinib exhibited lower IC50 values in the high-risk group, suggesting they may be more suitable for high-risk patients (Fig. S4G–N).

Single-cell sequencing analysis reveals the expression of five hub genes in ccRCC

We acquired the single-cell RNA sequencing dataset GSE224630 from the GEO database, comprising seven samples (RCC1-5, RCC4f, and RCC5t) obtained from five distinct ccRCC patients. Following rigorous quality control and data filtering procedures, we applied the Harmony package to mitigate batch effects during data integration (Fig. S5A-C). Our analysis identified 3,000 highly variable genes highlighted in red, with the top 10 most significant variable genes marked (Fig. S5D).

Through UMAP-based dimensionality reduction and clustering analysis of the seven tumor samples, we delineated 16 distinct cellular clusters (Fig. 6A-B). Systematic cell type annotation of these clusters revealed seven biologically relevant categories, achieved by leveraging established cell-type-specific marker genes such as *CA9* (epithelial/tumor cells), *PECAM1* (endothelial cells), and *PTPRC* (immune cells) (Fig. 6D, Fig. 6J). Notably, our analysis uncovered substantial inter-tumoral heterogeneity among the different patient samples (Fig. 6C). Subsequent expression profiling of five hub genes demonstrated cell-type-specific patterns: *KCNK5*, *PIK3R3*, and *TMCC3* showed predominant expression in endothelial cells, while *EPS8* localized primarily to pericytes. *TOP2A* exhibited significant expression in epithelial/tumor cell populations (Fig. S5E, Fig. 6E-I, Fig. 6K). These expression patterns were visualized across the identified cell types to illustrate their differential distribution.

KCNK5 is associated with the prognosis, clinical features, and immune infiltration in ccRCC

Our analysis of transcriptome data from the TCGA-KIRC and GEO datasets (GSE40435, GSE53757), encompassing both ccRCC and normal samples, revealed consistently low expression of *KCNK5* in ccRCC across multiple datasets (Fig. 7A-C). Survival analysis on the TCGA-KIRC, E-MTAB-1980, and ICGC-KIRC datasets demonstrated a significant association between reduced *KCNK5* expression levels and poorer patient prognosis in ccRCC (Fig. 7D-F). Further investigation into the correlation between *KCNK5* expression and clinical characteristics indicated that patients with lower *KCNK5* expression exhibited more advanced disease progression, as evidenced by higher histological grades, pathological T stages, and pathological M stages (Fig. 7G-I).Our examination of the relationship between *KCNK5* expression and immune cell infiltration in ccRCC revealed significant associations. *KCNK5* expression showed positive correlations with mast cells resting, dendritic cells resting, monocytes, NK cells activated, macrophages M1, and T cells CD8. Conversely, negative correlations were observed with Tregs, T cells gamma delta, mast cells activated, T cells CD4 memory activated, and macrophages M0 (Fig. 7J-L).Additionally, we conducted comprehensive analyses of the remaining four hub genes in TCGA-KIRC, focusing on their expression patterns, survival implications, and pathological T stages. These genes were found to be highly expressed in ccRCC. Notably, elevated *TOP2A* expression was associated with poorer prognosis in the tumor group, while reduced expression of *PIK3R3*, *EPS8*, and *TMCC3* correlated with worse outcomes. Furthermore, the downregulation of *PIK3R3* and upregulation of *TOP2A* were significantly linked to increased pathological T stage, whereas *EPS8* and *TMCC3* showed no such significant association (Fig. S6A-D).

Overexpression of KCNK5 inhibits the proliferation, migration, and invasion of ccRCC cell lines

We validated the downregulated mRNA levels of *KCNK5* in commonly used ccRCC cell lines and found that the protein levels of *KCNK5* in ccRCC tissues were lower than those in adjacent normal tissues (Fig. 8A-B). This is consistent with our previous findings reported in public databases. Subsequently, we established a ccRCC cell line overexpressing *KCNK5* (Fig. 8C-D) to investigate the biological function of *KCNK5* in ccRCC. CCK8 assay results indicated that *KCNK5* overexpression significantly inhibited the proliferative capacity of ccRCC cells (Fig. 8E-F). Additionally, EdU cell proliferation assays revealed that *KCNK5* overexpression significantly suppressed the proliferative activity of ccRCC cells (Fig. 8G-H). As demonstrated by cell wound healing experiments, compared with the control group, the *KCNK5*-overexpressing group exhibited larger wound areas at 12 and 24 hours post-wound, significantly delaying wound healing rates (Fig. 8I-J). Transwell migration and invasion experiments revealed that the migration and invasion capabilities of the *KCNK5*-overexpressing group were significantly reduced (Fig. 8K-L).

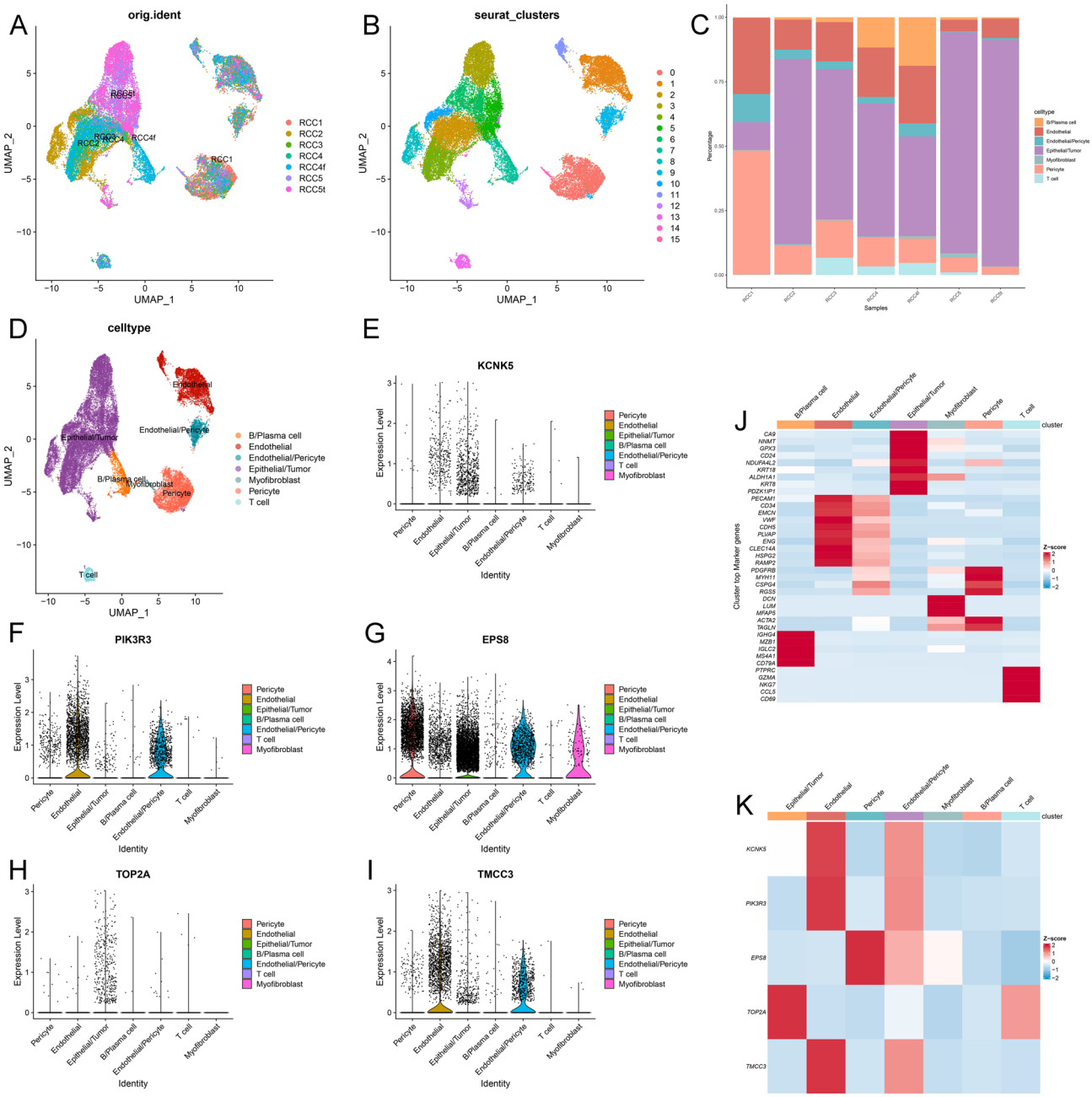

Figure. 6. ScRNA-seq analysis reveals the expression patterns of five model genes in ccRCC. (**A**) UMAP plot colored by Patient ID.(**B**) UMAP dimension reduction identifying 16 cell clusters. (**C**) Distribution of intratumoral heterogeneity across patients. (**D**) UMAP plot with manually annotated cell types. (**E–I, K**) Cell type-specific expression patterns of the five model genes: *KCNK5/PIK3R3/TMCC3* in endothelial cells, *EPS8* in pericytes, and *TOP2A* in epithelial/tumor cells. (**J**) Marker gene expression levels across seven cell types.

Discussion

As one of the most prevalent malignancies in the urinary system, ccRCC poses significant diagnostic challenges in its early stages due to its asymptomatic presentation. Frequent delays in detection frequently lead to advanced metastatic disease at initial diagnosis. While current therapeutic strategies including targeted agents and immunotherapies have demonstrated partial success in improving patient outcomes, substantial limitations persist[57]. The heterogeneous treatment responses among individuals and the inevitable development of drug resistance ultimately result in disease progression to metastatic ccRCC in a subset of patients[58]. As previously established, SCRGs play pivotal roles in ccRCC pathogenesis. Nevertheless, existing research has predominantly focused on single-subunit mutations within SCRCs, with a notable paucity of investigations addressing the polygenic characteristics associated with SCRGs.

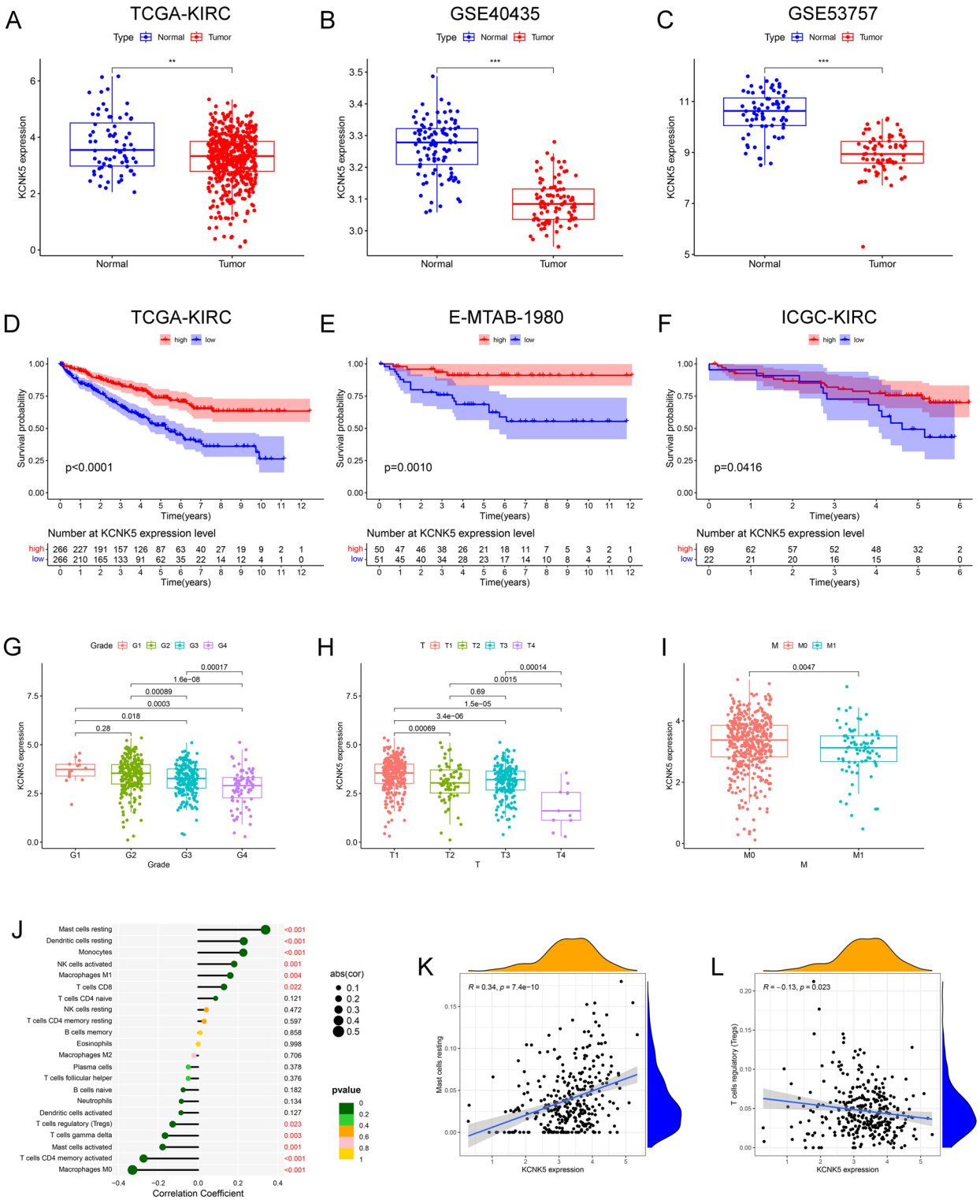

Figure. 7. Prognostic and immunomodulatory significance of *KCNK5* dysregulation in ccRCC. Reduced *KCNK5* expression in tumor specimens across TCGA-KIRC (**A**), GSE40435 (**B**), and GSE53757 (**C**) cohorts. Survival disadvantage associated with *KCNK5* underexpression in TCGA-KIRC (**D**), E-MTAB-1980 (**E**), and ICGC-KIRC (**F**) datasets. Clinicopathological correlations demonstrating *KCNK5* downregulation with advanced disease features: elevated histological grade (**G**), higher pathological T-stage (**H**), and metastatic progression (**I**). (**J**) The lollipop plot visualizes the association between *KCNK5* expression and immune cell infiltration in ccRCC. Significant negative relationship between *KCNK5* expression and Tregs infiltration (**K**), contrasting with a positive association with mast cells resting (**L**).

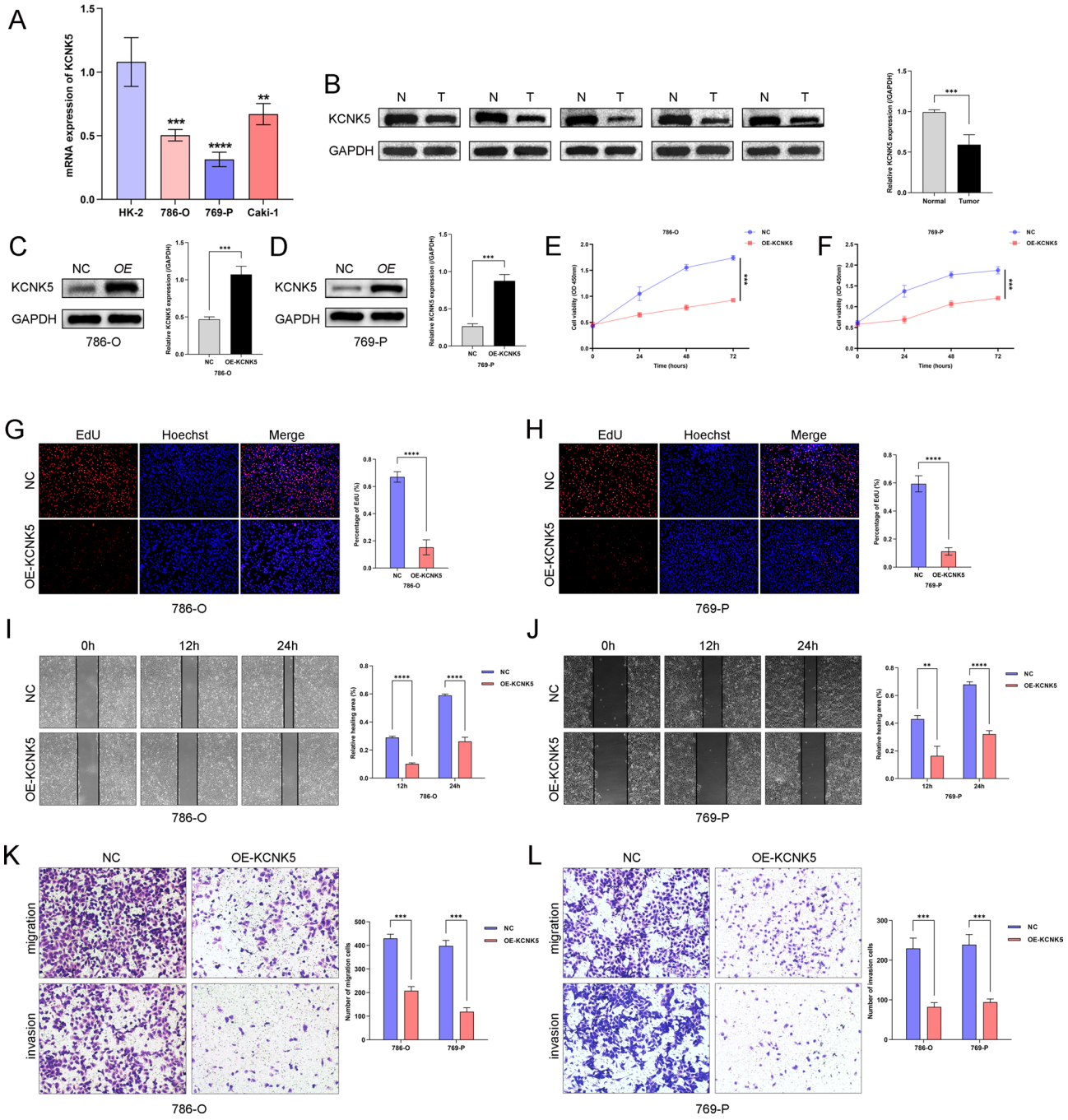

Figure. 8. Functional validation of *KCNK5* in ccRCC and its effects on cell proliferation, migration, and invasion. (**A–B**) *KCNK5* mRNA and protein expression were markedly downregulated in tumors. (**C–D**) *KCNK5*-overexpressing ccRCC cell lines were successfully established. (**E–H**) *KCNK5* overexpression significantly suppressed ccRCC cell proliferation. (**I–J**) The wound healing was delayed in the *KCNK5*-overexpressing group. (**K–L**) *KCNK5* overexpression significantly diminished the migration and invasion capabilities of ccRCC cells.

This investigation pioneers the stratification of ccRCC into two distinct molecular subtypes through unsupervised consensus clustering analysis of 29 SCRGs' expression profiles. Survival analysis revealed significantly worse clinical outcomes in cluster B than in cluster A. Intriguingly, tumor microenvironment characterization demonstrated markedly elevated immune cell infiltration relative to cluster A. Mechanistically, functional enrichment analyses implicated SCRGs in modulating critical oncogenic pathways such as EMT, *IL-6/JAK/STAT3* signaling, and fatty acid metabolic reprogramming, potentially driving clinical outcomes in ccRCC patients.

In recent years, single-cell sequencing technology has experienced rapid development[59]. Single-cell sequencing technology and analytical tools enable oncologists to gain deeper insights into the tumor immune microenvironment and its impact on anti-tumor immune responses[60]. Furthermore, by employing advanced single-cell sequencing techniques, we visualized the expression patterns of five model genes (TMCC3, TOP2A, EPS8, PIK3R3, KCNK5) in ccRCC tissues. Results revealed that, except for TOP2A, which showed higher expression in epithelial/tumor cells, the other four model genes exhibited elevated expression in endothelial/peritumoral cells. This suggests that these five model genes may be closely associated with the immune microenvironment of ccRCC. Based on these findings, we hold great promise for novel therapeutic approaches through immunotherapy.

Our machine learning-based 5-gene prognostic model (*TMCC3*, *TOP2A*, *EPS8*, *PIK3R3*, *KCNK5*) exhibited robust predictive performance across multiple independent cohorts. Survival analyses confirmed that elevated risk scores correlated significantly with poor clinical outcomes. ROC curve assessments demonstrated the model's strong prognostic accuracy for ccRCC patients, with consistent validation in both test and external cohorts. GSEA revealed significant enrichment of EMT and G2M-checkpoint pathways in high-risk subgroups. Univariate and multivariate Cox analyses established risk scores as independent prognostic factors for ccRCC outcomes. We further integrated clinical parameters with the prognostic model to construct a nomogram, whose AUC value on the ROC curve substantially outperformed conventional clinical features. Multi-algorithm immune profiling uncovered distinct risk-stratified TME characteristics: while high-risk groups showed increased CD8+ T cell and Tfh cell infiltration, this coexisted with Tregs accumulation and upregulated immune checkpoints, forming a paradoxical "immune activation-suppression" state. This unique immune phenotype may explain poor treatment responses in highly infiltrated tumors. Multiple studies indicate that high levels of $CD8^+$ T cell infiltration in ccRCC not only fail to predict favorable treatment responses but are instead associated with higher tumor grades, later stages, and poorer survival outcomes[61–64]. Consequently, a review article[65] reports that the immune microenvironment of ccRCC possesses unique suppressive mechanisms, preventing a large number of infiltrating T cells from effectively killing tumor cells. Despite its appearance of "high-level immune infiltration," it is internally filled with dysfunctional T cells, immunosuppressive cells (such as Tregs), heterogeneous tumor cells, and a metabolically disordered microenvironment. TIDE scoring indicated greater immune escape potential in high-risk patients, suggesting reduced immunotherapy efficacy[53]. Conversely, Drug sensitivity analysis demonstrated enhanced sensitivity to targeted therapies and immunotherapies in low-risk groups. These findings confirm our model's dual utility as both a prognostic predictor and TME biomarker while highlighting SCRGs' critical role in ccRCC progression and therapeutic resistance.

Existing research shows that the five model genes play a role in influencing various tumor processes via multiple mechanisms. *TMCC3*, a member of the transmembrane and helical domains family (*TMCCs*) is found in the endoplasmic reticulum[66]. Studies have reported that *TMCC3* enhances *AKT* activation, promoting the self-renewal and metastasis of breast cancer stem cells and leading to a poor breast cancer prognosis[67]. *TOP2A* regulates DNA topology during replication, transcription, and repair and is linked to various tumor malignancies[68]. In nasopharyngeal carcinoma, *KDM5B* indirectly upregulates *TOP2A* expression by demethylating the transcription start site histone H3K4, thus boosting cell proliferation, invasion, and cisplatin resistance[69]. Moreover, knocking down *TOP2A* considerably inhibits ccRCC cell proliferation and migration in experiments[70]. *EPS8*, initially identified as a substrate of tyrosine kinase receptors, is associated with malignant tumor phenotypes[71]. Studies indicate that silencing *EPS8* can suppress EMT and cell proliferation in enzalutamide-resistant prostate cancer cells[72]. Additionally, an inhibitory short peptide blocking the *SOS1/EPS8/ABI1* trimer interaction has been developed to curb ovarian cancer metastasis[73]. In pancreatic ductal adenocarcinoma, *EPS8* prevents *BMI1* mediated ubiquitin-proteasome degradation of *ALDH7A1*, thereby promoting tumor cell survival and proliferation[74]. *PIK3R3* encodes a regulatory subunit of phosphoinositide kinase[75]. Research shows that *PIK3R3* expression is elevated in colorectal cancer. However, high *PIK3R3* expression can activate the *NF-κB* pathway to regulate *TP* transcription levels, thereby promoting 5-fluorouracil-induced apoptosis[76]. Another study demonstrated that *PIK3R3* overexpression induces EMT, enhancing colorectal cancer cell migration and invasion and promoting in vivo tumor metastasis[77]. Furthermore, studies have shown that *PIK3R3* downregulation in *VHL*-deficient ccRCC leads to excessive *AKT* activation and tumor growth[78]. *KCNK5* encodes a member of the potassium channel protein superfamily and is mainly expressed in the renal cortex's distal convoluted tubules and collecting ducts[79]. Although studies have suggested that *KCNK5* may promote the proliferation of breast cancer cells[80] and may be associated with poor prognosis in thyroid cancer[81]. However, our findings indicate that *KCNK5* exerts a tumor-suppressive role in ccRCC. It is important to note that research has shown *KCNK5* upregulation inhibits autophagy and induces pyroptosis in dry eye syndrome by regulating *TNFSF10*[82]. Another study reported that *KCNK5* knockout improves renal fibrosis by reducing G2/M phase cell cycle arrest[83]. Therefore, we hypothesize that *KCNK5* may induce pyroptosis in ccRCC cells by affecting autophagy-related pathways or suppress proliferation by inducing G2/M phase cell cycle arrest. Our study found that except for *KCNK5*, the other four model genes are highly expressed in ccRCC. Interestingly, *KCNK5* is downregulated in ccRCC, and as its expression increases, the prognosis of ccRCC patients relatively improves. Clinical correlation analysis revealed that reduced *KCNK5* expression is associated with poorer clinical outcomes in ccRCC patients. However, no significant correlation was observed between the expression levels of *TMCC3* and *EPS8* and the staging of ccRCC patients in the clinical correlation analysis. *TOP2A* and *PIK3R3* have both been confirmed to influence ccRCC progression through different mechanisms. Therefore, we selected *KCNK5* as the target gene for further experimental studies to clarify its biological role in ccRCC prognosis.

First, our data confirmed that *KCNK5* expression is markedly downregulated in ccRCC cell lines and tissues, aligning with our prior bioinformatics findings. CCK-8 and EdU assay results showed that *KCNK5* overexpression significantly curbed ccRCC cell proliferation. Moreover, *KCNK5* overexpression reduced wound

healing rates in ccRCC cell lines and suppressed cell migration and invasion in Transwell assays. Overall, our study demonstrates that *KCNK5* overexpression inhibits ccRCC cell proliferation, migration, and invasion.

While our investigation leveraged multi-omics data from public repositories with systematic bioinformatics analysis and experimental validation, several limitations merit consideration. Our study primarily employed retrospective cohort analysis. While findings were validated in an independent cohort, limitations persist. First, we require additional prospective patient cohorts to validate our findings. Second, the interaction mechanisms between the SCRG prognostic model and tumor microenvironment infiltration and immune cell infiltration remain unclear, necessitating more experimental research. Finally, although we experimentally confirmed that *KCNK5* inhibits ccRCC cell proliferation, migration, and invasion, the exact signaling pathways and mechanisms require further exploration.

Conclusions

In summary, this study systematically revealed the role of SCRGs in the subtyping and prognosis of clear cell carcinoma through bioinformatics techniques. The two identified subtypes (SCRGcluster A and SCRGcluster B) exhibited significant differences in functional enrichment and tumor immune microenvironment infiltration. The constructed prognostic model demonstrated predictive efficacy in external validation datasets. Experimental validation further revealed that overexpression of *KCNK5* in ccRCC cell lines suppressed proliferative, migratory, and invasive capacities. Despite certain limitations, the identified core genes and preliminary experimental findings may provide new avenues for improving prognostic evaluation and treatment strategies in ccRCC. Future studies will focus on elucidating the precise molecular mechanisms involved, which may contribute to the development of novel therapeutic targets for ccRCC.

Data availability

All public datasets used in this study can be downloaded from the official websites. The original data could be obtained from the corresponding author upon reasonable request.

Received: 13 June 2025; Accepted: 20 October 2025
Published online: 21 November 2025

References

1. Young, M. et al. Renal cell carcinoma. *Lancet* **404**(10451), 476–491. https://doi.org/10.1016/S0140-6736(24)00917-6 (2024) (**Epub 2024 Jul 18 PMID: 39033764**).
2. Rose, T. L. & Kim, W. Y. Renal cell carcinoma: A review. *JAMA* **332**(12), 1001–1010. https://doi.org/10.1001/jama.2024.12848 (2024) (**PMID: 39196544**).
3. Hsieh, J. J. et al. Renal cell carcinoma. *Nat. Rev. Dis. Primer.* **9**(3), 17009. https://doi.org/10.1038/nrdp.2017.9.PMID:28276433 (2017) (**PMCID:PMC5936048**).
4. Bukavina, L. et al. Epidemiology of renal cell carcinoma: 2022 update. *Eur. Urol.* **82**(5), 529–542. https://doi.org/10.1016/j.eururo.2022.08.019 (2022) (**Epub 2022 Sep 10 PMID: 36100483**).
5. Escudier, B. et al. Renal cell carcinoma: ESMO clinical practice guidelines for diagnosis, treatment and follow-up†. *Ann. Oncol.* **30**(5), 706–720. https://doi.org/10.1093/annonc/mdz056 (2019) (**PMID: 30788497**).
6. Motzer, R. J. et al. Kidney cancer, version 3.2022, NCCN clinical practice guidelines in oncology. *J. Natl. Compr. Canc. Netw.* **20**(1), 71–90. https://doi.org/10.6004/jnccn.2022.0001 (2022) (**PMID:34991070;PMCID:PMC10191161**).
7. Ljungberg, B. et al. European association of urology guidelines on renal cell carcinoma: The 2022 update. *Eur. Urol.* **82**(4), 399–410. https://doi.org/10.1016/j.eururo.2022.03.006 (2022) (**Epub 2022 Mar 26 PMID: 35346519**).
8. Ernst, M. S. et al. Outcomes for international metastatic renal cell carcinoma database consortium prognostic groups in contemporary first-line combination therapies for metastatic renal cell carcinoma. *Eur. Urol.* **84**(1), 109–116. https://doi.org/10.1016/j.eururo.2023.01.001 (2023) (**Eur Urol. 2023 Jul;84(1):109-116. 10.1016/j.eururo.2023.01.001. Epub 2023 Jan 26. Erratum in: Eur Urol. 2023 Jun;83(6):e166-e167. 10.1016/j.eururo.2023.03.003. PMID: 36707357**).
9. Motzer, R. et al. Lenvatinib plus pembrolizumab or everolimus for advanced renal cell carcinoma. *N. Engl. J. Med.* **384**(14), 1289–1300. https://doi.org/10.1056/NEJMoa2035716 (2021) (**Epub 2021 Feb 13 PMID: 33616314**).
10. Choueiri, T. K. et al. Nivolumab plus cabozantinib versus sunitinib for advanced renal-cell carcinoma. *N. Engl. J. Med.* **384**(9), 829–841. https://doi.org/10.1056/NEJMoa2026982 (2021) (**PMID:33657295;PMCID:PMC8436591**).
11. Rini, B. I. et al. Pembrolizumab plus axitinib versus sunitinib for advanced renal-cell carcinoma. *N. Engl. J. Med.* **380**(12), 1116–1127. https://doi.org/10.1056/NEJMoa1816714 (2019) (**Epub 2019 Feb 16 PMID: 30779529**).
12. Motzer, R. J. et al. Nivolumab plus ipilimumab versus sunitinib in advanced renal-cell carcinoma. *N. Engl. J. Med.* **378**(14), 1277–1290. https://doi.org/10.1056/NEJMoa1712126 (2018) (**PMID:29562145;PMCID:PMC5972549**).
13. Osterman, C. K., Deal, A. M., Milowsky, M. I., Bjurlin, M. A. & Rose, T. L. Trends in initial systemic therapy for elderly patients with metastatic clear cell renal cell carcinoma. *Kidney Cancer.* **4**(3), 131–137. https://doi.org/10.3233/KCA-200089 (2020) (**PMID :33195888;PMCID:PMC7605347**).
14. Mittal, P. & Roberts, C. W. M. The SWI/SNF complex in cancer - biology, biomarkers and therapy. *Nat. Rev. Clin. Oncol.* **17**(7), 435–448. https://doi.org/10.1038/s41571-020-0357-3 (2020) (**PMID:32303701;PMCID:PMC8723792**).
15. Malone, H. A. & Roberts, C. W. M. Chromatin remodellers as therapeutic targets. *Nat. Rev. Drug Discov.* **23**(9), 661–681. https://doi.org/10.1038/s41573-024-00978-5 (2024) (**PMID:39014081;PMCID:PMC11534152**).
16. Versteege, I. et al. Truncating mutations of hSNF5/INI1 in aggressive paediatric cancer. *Nature* **394**(6689), 203–6. https://doi.org/10.1038/28212 (1998) (**PMID: 9671307**).
17. Jones, S. et al. Frequent mutations of chromatin remodeling gene ARID1A in ovarian clear cell carcinoma. *Science* **330**(6001), 228–31. https://doi.org/10.1126/science.1196333PMID:20826764;PMCID:PMC3076894 (2010).
18. Wiegand, K. C. et al. ARID1A mutations in endometriosis-associated ovarian carcinomas. *N. Engl. J. Med.* **363**(16), 1532–43. https://doi.org/10.1056/NEJMoa1008433 (2010) (**PMID:20942669;PMCID:PMC2976679**).
19. Varela, I. et al. Exome sequencing identifies frequent mutation of the SWI/SNF complex gene PBRM1 in renal carcinoma. *Nature* **469**(7331), 539–42. https://doi.org/10.1038/nature09639 (2011) (**Epub 2011 Jan 19. Erratum in: Nature. 2012 Apr 5;484(7392):130. PMID: 21248752; PMCID: PMC3030920**).
20. Concepcion, C. P. et al. Smarca4 inactivation promotes lineage-specific transformation and early metastatic features in the lung. *Cancer Discov.* **12**(2), 562–585. https://doi.org/10.1158/2159-8290.CD-21-0248 (2022) (**Epub 2021 Sep 24. PMID: 34561242; PMCID: PMC8831463**).

21. Farnaby, W. et al. BAF complex vulnerabilities in cancer demonstrated via structure-based PROTAC design. *Nat. Chem. Biol.* **15**(7), 672–680. https://doi.org/10.1038/s41589-019-0294- (2019) (**6 Epub 2019 Jun 10. Erratum in: Nat Chem Biol. 2019 Aug; 15(8):846. 10.1038/s41589-019-0329-z. PMID: 31178587; PMCID: PMC6600871**).
22. Kim, K. H. et al. SWI/SNF-mutant cancers depend on catalytic and non-catalytic activity of EZH2. *Nat. Med.* **21**(12), 1491–6. https://doi.org/10.1038/nm.3968 (2015) (**Epub 2015 Nov 9 PMID: 26552009; PMCID: PMC4886303**).
23. Kim, K. H. & Roberts, C. W. Targeting EZH2 in cancer. *Nat. Med.* **22**(2), 128–34. https://doi.org/10.1038/nm.4036 (2016) (**PMID :26845405;PMCID:PMC4918227**).
24. Italiano, A. et al. Tazemetostat, an EZH2 inhibitor, in relapsed or refractory B-cell non-hodgkin lymphoma and advanced solid tumours: A first-in-human, open-label, phase 1 study. *Lancet Oncol.* **19**(5), 649–659. https://doi.org/10.1016/S1470-2045(18)30145-1 (2018) (**Epub 2018 Apr 9 PMID: 29650362**).
25. Mohammad, H. P., Barbash, O. & Creasy, C. L. Targeting epigenetic modifications in cancer therapy: Erasing the roadmap to cancer. *Nat. Med.* **25**(3), 403–418. https://doi.org/10.1038/s41591-019-0376-8 (2019) (**Epub 2019 Mar 6 PMID: 30842676**).
26. Zhuang, K. et al. Assessment of SWI/SNF chromatin remodeling complex related genes as potential biomarkers and therapeutic targets in pan-cancer. *Mol. Cancer.* **23**(1), 176. https://doi.org/10.1186/s12943-024-02015-w (2024) (**PMID: 39192265; PMCID: PMC11348550**).
27. Huang, J., Mao, L., Lei, Q. & Guo, A. Y. Bioinformatics tools and resources for cancer and application. *Chin Med J (Engl)* **137**(17), 2052–2064. https://doi.org/10.1097/CM9.0000000000003254 (2024) (**Epub 2024 Jul 30. PMID: 39075637; PMCID: PMC11374212**).
28. Zhang, C. et al. Aberrant activation of m6A demethylase FTO renders HIF2αlow/- clear cell renal cell carcinoma sensitive to BRD9 inhibitors. *Sci. Transl. Med.* https://doi.org/10.1126/scitranslmed.abf6045 (2021) (**Epub 2021 Sep 29. Erratum in: Sci Transl Med. 2023 Jun 28;15(702): eadj2190. 10.1126/scitranslmed.adj2190. PMID: 34586831**).
29. Cui, H. et al. The SWI/SNF chromatin remodeling factor DPF3 regulates metastasis of ccRCC by modulating TGF-β signaling. *Nat. Commun.* **13**(1), 4680. https://doi.org/10.1038/s41467-022-32472-0 (2022) (**PMID: 35945219; PMCID: PMC9363427**).
30. Carril-Ajuria, L., Santos, M., Roldán-Romero, J. M., Rodriguez-Antona, C. & de Velasco, G. Prognostic and predictive value of PBRM1 in clear cell renal cell carcinoma. *Cancers (Basel).* **12**(1), 16. https://doi.org/10.3390/cancers12010016 (2019) (**PMID: 31861590; PMCID: PMC7016957**).
31. Tang, Y. et al. PBRM1 deficiency oncogenic addiction is associated with activated AKT-mTOR signalling and aerobic glycolysis in clear cell renal cell carcinoma cells. *J. Cell Mol. Med.* **26**(14), 3837–3849. https://doi.org/10.1111/jcmm.17418 (2022) (**Epub 2022 Jun 7. PMID: 35672925; PMCID: PMC9279584**).
32. Hrizat, A. S. et al. Tumor infiltrating T-cells and loss of expression of SWI/SNF genes in varying stages of clear cell renal cell carcinoma. *Pathol. Res. Pract.* **266**, 155774. https://doi.org/10.1016/j.prp.2024.155774 (2025) (**Epub 2024 Dec 12 PMID: 39693721**).
33. Grossman, R. L. et al. Toward a shared vision for cancer genomic data. *N. Engl. J. Med.* **375**(12), 1109–12. https://doi.org/10.1056/NEJMp1607591.PMID:27653561;PMCID:PMC6309165 (2016).
34. Cancer Genome Atlas Research Network. Comprehensive molecular characterization of clear cell renal cell carcinoma. *Nature* https://doi.org/10.1038/nature12222 (2013) (**Epub 2013 Jun 23. PMID: 23792563; PMCID: PMC3771322**).
35. Parkinson, H. et al. ArrayExpress–a public database of microarray experiments and gene expression profiles. Nucl. Acid. Res. (Database issue) https://doi.org/10.1093/nar/gkl995 (2007) (**Epub 2006 Nov 28. PMID: 17132828; PMCID: PMC1716725**).
36. Sato, Y. et al. Integrated molecular analysis of clear-cell renal cell carcinoma. *Nat. Genet.* **45**(8), 860–7. https://doi.org/10.1038/ng.2699 (2013) (**Epub 2013 Jun 24 PMID: 23797736**).
37. Barrett, T. et al. NCBI GEO: Archive for functional genomics data sets–update. *Nucl. Acid. Res.* **41**(D1), D991-5. https://doi.org/10.1093/nar/gks1193 (2013) (**Epub 2012 Nov 27. PMID: 23193258; PMCID: PMC3531084**).
38. Ho, T. H. et al. Differential gene expression profiling of matched primary renal cell carcinoma and metastases reveals upregulation of extracellular matrix genes. *Ann. Oncol.* **28**(3), 604–610. https://doi.org/10.1093/annonc/mdw652.PMID:27993815;PMCID:PMC5834119 (2017).
39. Wozniak, M. B. et al. Integrative genome-wide gene expression profiling of clear cell renal cell carcinoma in Czech Republic and in the United States. *PLoS One* **8**(3), e57886. https://doi.org/10.1371/journal.pone.0057886 (2013) (**Epub 2013 Mar 5. PMID: 23526956; PMCID: PMC3589490**).
40. Herrem, C. J. et al. Expression of EphA2 is prognostic of disease-free interval and overall survival in surgically treated patients with renal cell carcinoma. *Clin. Cancer Res.* **11**(1), 226–31 (2005) (**PMID: 15671550**).
41. Saout, J. R. et al. Single-cell deconvolution of a specific malignant cell population as a poor prognostic biomarker in low-risk clear cell renal cell carcinoma patients. *Eur. Urol.* **83**(5), 441–451. https://doi.org/10.1016/j.eururo.2023.02.008 (2023) (**Epub 2023 Feb 15 PMID: 36801089**).
42. Mayakonda, A., Lin, D. C., Assenov, Y., Plass, C. & Koeffler, H. P. Maftools: Efficient and comprehensive analysis of somatic variants in cancer. *Genome. Res.* **28**(11), 1747–1756. https://doi.org/10.1101/gr.239244.118 (2018) (**Epub 2018 Oct 19. PMID: 30341162; PMCID: PMC6211645**).
43. Engebretsen, S. & Bohlin, J. Statistical predictions with glmnet. clin. *Epigenetics.* **11**(1), 123. https://doi.org/10.1186/s13148-019-0730-1 (2019) (**PMID:31443682;PMCID:PMC6708235**).
44. Alderden, J. et al. Predicting pressure injury in critical care patients: A machine-learning model. *Am. J. Crit. Care.* **27**(6), 461–468. https://doi.org/10.4037/ajcc2018525.PMID:30385537;PMCID:PMC6247790 (2018).
45. Yuan, K. C. et al. The development an artificial intelligence algorithm for early sepsis diagnosis in the intensive care unit. *Int. J. Med. Inform.* **141**, 104176. https://doi.org/10.1016/j.ijmedinf.2020.104176 (2020) (**Epub 2020 May 21 PMID: 32485555**).
46. Vickers, A. J., Cronin, A. M., Elkin, E. B. & Gonen, M. Extensions to decision curve analysis, a novel method for evaluating diagnostic tests, prediction models and molecular markers. *BMC Med. Inform. Decis. Mak.* **26**(8), 53. https://doi.org/10.1186/1472-6947-8-53.PMID:19036144;PMCID:PMC2611975 (2008).
47. Miao, Y. et al. Comprehensive characterization of RNA-binding proteins in colon adenocarcinoma identifies a novel prognostic signature for predicting clinical outcomes and immunotherapy responses based on machine learning. *Comb. Chem. High Throughput. Screen.* **26**(1), 163–182. https://doi.org/10.2174/1386207325666220404125228 (2023) (**PMID: 35379120**).
48. Subramanian, A. et al. Gene set enrichment analysis: A knowledge-based approach for interpreting genome-wide expression profiles. *Proc. Natl. Acad. Sci. U S A* **102**(43), 15545–50. https://doi.org/10.1073/pnas.0506580102 (2005) (**Epub 2005 Sep 30. PMID: 16199517; PMCID: PMC1239896**).
49. Kanehisa, M., Furumichi, M., Sato, Y., Kawashima, M. & Ishiguro-Watanabe, M. KEGG for taxonomy-based analysis of pathways and genomes. *Nucl. Acid. Res.* **51**(D1), D587–D592. https://doi.org/10.1093/nar/gkac963.PMID:36300620;PMCID:PMC9825424 (2023).
50. Newman, A. M. et al. Robust enumeration of cell subsets from tissue expression profiles. *Nat. Method.* **12**(5), 453–7. https://doi.org/10.1038/nmeth.3337 (2015) (**Epub 2015 Mar 30. PMID: 25822800; PMCID: PMC4739640**).
51. Yoshihara, K. et al. Inferring tumour purity and stromal and immune cell admixture from expression data. *Nat. Commun.* **4**, 2612. https://doi.org/10.1038/ncomms3612.PMID:24113773;PMCID:PMC3826632 (2013).
52. Thorsson, V. et al. The Immune landscape of cancer. *Immunity* **48**(4), 812-830.e14. https://doi.org/10.1016/j.immuni.2018.03.023 (2018) (**Epub 2018 Apr 5. Erratum in: Immunity. 2019 Aug 20;51(2):411-412. 10.1016/j.immuni.2019.08.004. PMID: 29628290; PMCID: PMC5982584**).

53. Jiang, P. et al. Signatures of T cell dysfunction and exclusion predict cancer immunotherapy response. *Nat. Med.* **24**(10), 1550–1558. https://doi.org/10.1038/s41591-018-0136-1 (2018) (**Epub 2018 Aug 20. PMID: 30127393; PMCID: PMC6487502**).
54. Maeser, D., Gruener, R. F. & Huang, R. S. oncoPredict: An R package for predicting in vivo or cancer patient drug response and biomarkers from cell line screening data. *Brief. Bioinform.* https://doi.org/10.1093/bib/bbab260 (2021).
55. Satija, R., Farrell, J. A., Gennert, D., Schier, A. F. & Regev, A. Spatial reconstruction of single-cell gene expression data. *Nat. Biotechnol.* **33**(5), 495–502. https://doi.org/10.1038/nbt.3192 (2015) (**Epub 2015 Apr 13. PMID: 25867923; PMCID: PMC4430369**).
56. Becht, E. et al. Newell EWJNb: Dimensionality reduction for visualizing single-cell data using UMAP. *Nat. Biotech.* **37**(1), 38–44 (2019).
57. Chakiryan, N. H. et al. Real-world survival outcomes associated with first-line immunotherapy, targeted therapy, and combination therapy for metastatic clear cell renal cell carcinoma. *JAMA Netw. Open.* **4**(5), e2111329. https://doi.org/10.1001/jamanetworkopen.2021.11329 (2021) (**PMID:34032854;PMCID:PMC8150693**).
58. Marona, P. et al. MCPIP1 downregulation in clear cell renal cell carcinoma promotes vascularization and metastatic progression. *Cancer Res.* **77**(18), 4905–4920. https://doi.org/10.1158/0008-5472.CAN-16-3190 (2017) (**Epub 2017 Jul 17 PMID: 28716897**).
59. Xu, J., Liao, K., Yang, X., Wu, C. & Wu, W. Correction to: Using single-cell sequencing technology to detect circulating tumor cells in solid tumors. *Mol. Cancer.* **21**(1), 100. https://doi.org/10.1186/s12943-022-01564-2 (2022) (**Erratumfor:MolCancer.2021Aug19;20(1):104.doi:10.1186/s12943-021-01392-w.PMID:35436930;PMCID:PMC9014560**).
60. Jia, Q., Chu, H., Jin, Z., Long, H. & Zhu, B. High-throughput single-cell sequencing in cancer research. *Signal Transduct. Target Ther.* **7**(1), 145. https://doi.org/10.1038/s41392-022-00990-4.PMID:35504878;PMCID:PMC9065032 (2022).
61. Jansen, C. S. et al. An intra-tumoral niche maintains and differentiates stem-like CD8 T cells. *Nature* **576**(7787), 465–470. https://doi.org/10.1038/s41586-019-1836-5 (2019) (**Epub 2019 Dec 11. PMID: 31827286; PMCID: PMC7108171**).
62. Clark, D. J. et al. Integrated proteogenomic characterization of clear cell renal cell carcinoma. *Cell.* **179**(4), 964-983.e31. https://doi.org/10.1016/j.cell.2019.10.007 (2019) (**Erratum.In:Cell.2020Jan9;180(1):207.doi:10.1016/j.cell.2019.12.026.PMID:31675502; PMCID:PMC7331093**).
63. Qi, Y. et al. Tumor-infiltrating $CD39^{+}CD8^{+}$ T cells determine poor prognosis and immune evasion in clear cell renal cell carcinoma patients. *Cancer Immunol. Immunother.* **69**(8), 1565–1576. https://doi.org/10.1007/s00262-020-02563-2 (2020) (**Epub 2020 Apr 18. PMID: 32306075; PMCID: PMC11027701**).
64. Wu, X. et al. $CD8^{+}$ T cell-based molecular classification with heterogeneous immunogenomic landscapes and clinical significance of clear cell renal cell carcinoma. *Front. Immunol.* **14**(12), 745945. https://doi.org/10.3389/fimmu.2021.745945.PMID:34970257;PMCID:PMC8713701 (2021).
65. Burgers, F. H. et al. Immunological features of clear-cell renal-cell carcinoma and resistance to immune checkpoint inhibitors. *Nat. Rev. Nephrol.* https://doi.org/10.1038/s41581-025-00983-w (2025) (**Epub ahead of print. PMID: 40696159**).
66. Sohn, W. J. et al. Expression and characterization of transmembrane and coiled-coil domain family 3. *BMB Rep.* **49**(11), 629–634. https://doi.org/10.5483/bmbrep.2016.49.11.151.PMID:27697108;PMCID:PMC5346324 (2016).
67. Wang, Y. H. et al. Transmembrane and coiled-coil domain family 3 (TMCC3) regulates breast cancer stem cell and AKT activation. *Oncogene* **40**(16), 2858–2871. https://doi.org/10.1038/s41388-021-01729-1 (2021) (**Epub 2021 Mar 19. PMID: 33742122; PMCID: PMC8062265**).
68. Pilati, P., Nitti, D. & Mocellin, S. Cancer resistance to type II topoisomerase inhibitors. *Curr. Med. Chem.* **19**(23), 3900–6. https://doi.org/10.2174/092986712802002473 (2012) (**PMID: 22788766**).
69. Zhang, B. et al. Deubiquitinase USP7 stabilizes KDM5B and promotes tumor progression and cisplatin resistance in nasopharyngeal carcinoma through the ZBTB16/TOP2A axis. *Cell Death Differ.* **31**(3), 309–321. https://doi.org/10.1038/s41418-024-01257-x (2024) (**Epub 2024 Jan 29. PMID: 38287116; PMCID: PMC10923876**).
70. Wang, Q. et al. Assessing the role of programmed cell death signatures and related gene TOP2A in progression and prognostic prediction of clear cell renal cell carcinoma. *Cancer Cell Int.* **24**(1), 164. https://doi.org/10.1186/s12935-024-03346-w (2024) (**PMID:38730293;PMCID:PMC11084013**).
71. Luo, K. et al. Effects and mechanisms of Eps8 on the biological behaviour of malignant tumours (Review). *Oncol. Rep.* **45**(3), 824–834. https://doi.org/10.3892/or.2021.7927 (2021) (**Epub 2021 Jan 7. PMID: 33432368; PMCID: PMC7859916**).
72. Huang, W. L. et al. Knockdown of EPS8 expression attenuates the proliferation of enzalutamide-resistant prostate cancer cells. *Am. J. Cancer Res.* **14**(10), 4717–4730. https://doi.org/10.62347/YQWJ7498 (2024) (**PMID:39553210;PMCID:PMC11560819**).
73. Yu, X., Liang, C., Zhang, Y., Zhang, W. & Chen, H. Inhibitory short peptides targeting EPS8/ABI1/SOS1 tri-complex suppress invasion and metastasis of ovarian cancer cells. *BMC Cancer* **19**(1), 878. https://doi.org/10.1186/s12885-019-6087-1 (2019) (**PMID:31488087;PMCID:PMC6727365**).
74. Tan, M., Meng, J., Sun, X., Fu, X. & Wang, R. EPS8 supports pancreatic cancer growth by inhibiting BMI1 mediated proteasomal degradation of ALDH7A1. *Exp. Cell Res.* **407**(1), 112782. https://doi.org/10.1016/j.yexcr.2021.112782 (2021) (**Epub 2021 Aug 13. PMID: 34391775**).
75. Pons, S. et al. The structure and function of p55PIK reveal a new regulatory subunit for phosphatidylinositol 3-kinase. *Mol. Cell Biol.* **15**(8), 4453–65. https://doi.org/10.1128/MCB.15.8.4453 (1995) (**PMID:7542745;PMCID:PMC230685**).
76. Ibrahim, S. et al. PIK3R3 promotes chemotherapeutic sensitivity of colorectal cancer through PIK3R3/NF-kB/TP pathway. *Cancer Biol. Ther.* https://doi.org/10.1080/15384047.2017.1416936 (2018) (**Epub 2018 Jan 25. PMID: 29370570; PMCID: PMC5790378**).
77. Wang, G. et al. PIK3R3 induces epithelial-to-mesenchymal transition and promotes metastasis in colorectal cancer. *Mol. Cancer Ther.* **13**(7), 1837–47. https://doi.org/10.1158/1535-7163.MCT-14-0049 (2014) (**Epub 2014 May 16 PMID: 24837077**).
78. Lee, H., Zhuang, L. & Gan, B. VHL governs m6A modification and PIK3R3 mRNA stability in clear cell renal cell carcinomas. *J. Clin. Invest.* **134**(8), e179560. https://doi.org/10.1172/JCI179560 (2024) (**PMID:38618953;PMCID:PMC11014664**).
79. Reyes, R. et al. Cloning and expression of a novel pH-sensitive two pore domain K+ channel from human kidney. *J. Biol. Chem.* **273**(47), 30863–9. https://doi.org/10.1074/jbc.273.47.30863 (1998) (**PMID: 9812978**).
80. Alvarez-Baron, C. P., Jonsson, P., Thomas, C., Dryer, S. E. & Williams, C. The two-pore domain potassium channel KCNK5: induction by estrogen receptor alpha and role in proliferation of breast cancer cells. *Mol. Endocrinol.* **25**(8), 1326–36. https://doi.org/10.1210/me.2011-0045 (2011) (**Epub 2011 Jun 16. PMID: 21680658; PMCID: PMC3146246**).
81. Lin, X. et al. The correlation and role analysis of KCNK2/4/5/15 in human papillary thyroid carcinoma microenvironment. *J. Cancer.* **11**(17), 5162–5176. https://doi.org/10.7150/jca.45604b (2020) (**PMID:32742463;PMCID:PMC7378911**).
82. Liao, K. et al. KCNK5 regulating potassium efflux and inducing pyroptosis in corneal epithelial cells through TNFSF10-mediated autophagy in dry eye. *Invest. Ophthalmol. Vis. Sci.* **65**(1), 34. https://doi.org/10.1167/iovs.65.1.34 (2024) (**PMID:38236186;PMCID:PMC10807492**).
83. Zhang, J. et al. TWIK-related acid-sensitive K+ channel 2 promotes renal fibrosis by inducing cell-cycle arrest. *iScience* https://doi.org/10.1016/j.isci.2022.105620 (2022) (**PMID: 36465115; PMCID: PMC9712759**).
84. Kanehisa, M., Furumichi, M., Sato, Y., Matsuura, Y. & Ishiguro-Watanabe, M. KEGG: Biological systems database as a model of the real world. *Nucl. Acid. Res.* **53**(D1), D672–D677. https://doi.org/10.1093/nar/gkae909 (2025) (**PMID:39417505; PMCID:PMC11701520**).
85. Kanehisa, M. Toward understanding the origin and evolution of cellular organisms. *Protein Sci* **28**(11), 1947–1951. https://doi.org/10.1002/pro.3715 (2019) (**PMID: 31441146; PMCID: PMC6798127**).
86. Kanehisa, M. & Goto, S. KEGG: kyoto encyclopedia of genes and genomes. *Nucl. Acid. Res.* **28**(1), 27–30. https://doi.org/10.1093/nar/28.1.27 (2000) (**PMID:10592173;PMCID:PMC102409**).

Acknowledgments
All authors would like to express their sincere gratitude to the developers of the public databases used in this study.

Author contributions
KX, ZY, and YL participated in the conception and design of this study. QQ and XN provided technical support. HT was responsible for data collection and analysis. KX and ZY were responsible for the experimental operations. KX and YL drafted the first version of the manuscript. LW, ZC, and XL revised and edited the manuscript. All authors reviewed and approved the final version of the manuscript.

Funding
This study was supported by the National Natural Science Foundation of China (No.82372200).

Declarations

Conflict of interest
All authors have no conflicts of interest or financial ties to disclose.

Ethics
This study was approved by the Renmin Hospital of Wuhan University Clinical Research Ethics Committee (approval number: WDRY2023-K176) and conducted in accordance with the Declaration of Helsinki. As the study was retrospective, it was exempt from informed consent requirements.

Informed consent
The Renmin Hospital of Wuhan University Clinical Research Ethics Committee approved the study (approval number: WDRY2023-K176) and waived the requirement for informed consent due to the retrospective nature of the study.

Additional information
Supplementary Information The online version contains supplementary material available at https://doi.org/10.1038/s41598-025-25283-y.

Correspondence and requests for materials should be addressed to L.W., Z.C. or X.L.